Planetary and Space Science 156 (2018) 23–40

Contents lists available at ScienceDirect

Planetary and Space Science

journal homepage: www.elsevier.com/locate/pss

SELMA mission: How do airless bodies interact with space environment? The Moon as an accessible laboratory

Yoshifumi Futaana [a,*], Stas Barabash [a], Martin Wieser [a], Peter Wurz [b], Dana Hurley [c], Mihaly Horányi [d], Urs Mall [e], Nicolas Andre [f], Nickolay Ivchenko [g], Jürgen Oberst [h], Kurt Retherford [i], Andrew Coates [j], Adam Masters [k], Jan-Erik Wahlund [l], Esa Kallio [m], SELMA proposal team

[a] Swedish Institute of Space Physics, Box 812, Kiruna, SE 98128, Sweden
[b] University of Bern, Bern, Switzerland
[c] The Johns Hopkins University Applied Physics Laboratory, Laurel, USA
[d] Laboratory for Atmospheric and Space Physics, University of Colorado, USA
[e] Max Planck Institute for Solar System Research, Göttingen, Germany
[f] IRAP- Université de Toulouse, CNRS, France
[g] KTH Royal Institute of Technology, Stockholm, Sweden
[h] German Aerospace Center, Berlin, Germany
[i] Southwest Research Institute, San Antonio, USA
[j] Mullard Space Science Laboratory, University College London, London, UK
[k] Imperial College London, London, UK
[l] Swedish Institute of Space Physics, Uppsala, Sweden
[m] Aalto University, Helsinki, Finland

ARTICLE INFO

Keywords:
Moon exploration
Volatile
Water
Mini-magnetosphere
Dust
Permanently shadowed crater

ABSTRACT

The Moon is an archetypal atmosphere-less celestial body in the Solar System. For such bodies, the environments are characterized by complex interaction among the space plasma, tenuous neutral gas, dust and the outermost layer of the surface. Here we propose the SELMA mission (Surface, Environment, and Lunar Magnetic Anomalies) to study how airless bodies interact with space environment. SELMA uses a unique combination of remote sensing via ultraviolet and infrared wavelengths, and energetic neutral atom imaging, as well as in situ measurements of exospheric gas, plasma, and dust at the Moon. After observations in a lunar orbit for one year, SELMA will conduct an impact experiment to investigate volatile content in the soil of the permanently shadowed area of the Shackleton crater. SELMA also carries an impact probe to sound the Reiner-Gamma mini-magnetosphere and its interaction with the lunar regolith from the SELMA orbit down to the surface. SELMA was proposed to the European Space Agency as a medium-class mission (M5) in October 2016. Research on the SELMA scientific themes is of importance for fundamental planetary sciences and for our general understanding of how the Solar System works. In addition, SELMA outcomes will contribute to future lunar explorations through qualitative characterization of the lunar environment and, in particular, investigation of the presence of water in the lunar soil, as a valuable resource to harvest from the lunar regolith.

1. Introduction

The Moon, Phobos, Deimos, and the majority of planetary satellites, Mercury, dwarf planets, and asteroids do not possess atmospheres. Solar radiation, space plasmas, meteoroids, and dust directly access the surface, changing its properties (called space weathering) and resulting in an environment where four main components, plasma, neutral gas, dust, and the outermost layer of the surface interact with each other in a very complex way. In order to investigate these interactions, we have designed a new-generation lunar mission, SELMA (Surface, Environment, and Lunar Magnetic Anomalies).

The mission SELMA was proposed in response to *the call for a Medium-*

* Corresponding author.
E-mail address: futaana@irf.se (Y. Futaana).

https://doi.org/10.1016/j.pss.2017.11.002
Received 31 July 2017; Received in revised form 7 October 2017; Accepted 1 November 2017
Available online 3 November 2017

size Mission Opportunity in European Space Agency's (ESA) science program (M5). SELMA is a mission in the frame of the Cosmic Vision themes "1. What are the conditions for planet formation and the emergence of life?" and "2. How does the Solar System work?" (Cosmic Vision, 2005). SELMA addresses the Cosmic Vision topics "1.3 Life and habitability in the Solar System" and "2.3 Asteroids and other small bodies".

The science question of SELMA is "How do airless bodies interact with space environment?" SELMA studies the Moon, an archetypal airless celestial body in the Solar System. SELMA studies water, one of the main ingredients for the life as we know it. SELMA will reveal the mechanisms of the water/hydroxyl formation on regolith-covered surfaces. While such bodies hardly can or could have been habitable, general studies how water is created, transported, stored, and escapes are an important contribution to understanding the fate of water in the solar system. SELMA also studies how airless bodies and small magnetic structures (magnetic anomalies) interact with the solar wind plasma, how surface bounded exospheres are created and maintained, and how the dust environment works; details of the scientific objectives are described in Section 2. All these results are of fundamental importance for planetary science and can be applicable throughout the solar system including the moons of Jupiter and Saturn, asteroids and dwarf planets.

In order to realize the science objectives, SELMA comprises of the SELMA orbiter, SELMA impact probe for Magnetic Anomaly (SIP-MA), passive impactor (10 kg copper sphere), and a relay CubeSat (RCS). The SELMA orbiter and SIP-MA host scientific instruments. The SELMA orbiter carries four remote sensing instruments and seven in-situ instruments. SIP-MA is equipped with four scientific instruments. The SELMA mission's lifetime is 15 months. The launch time is flexible, while the proposed SELMA mission complies with the requirement of ESA's M5 mission time line, i.e., aiming at 2029. The SELMA orbiter is inserted into a lunar polar orbit, nominally with a pericenter at 30 km and an apocenter at 200 km above the surface, for collecting the scientific data for the whole mission period. Two different measurement campaigns are conducted. An impact probe experiment using SIP-MA to investigate the lunar mini-magnetosphere is done 6 months after the launch; while the timing is flexible. The opportunity for SIP-MA is once a month. The second experiment will be done at the end of the mission: A passive impactor will be released aiming at a permanently shadowed region (the Shackleton crater is the baseline) to create an impact plume, which will be measured both remotely and locally by the SELMA orbiter. The SELMA orbiter chases the passive impactor along almost the identical orbit with a full science operation, and it crashes to the closer location to the passive impactor. Details of the mission description and instrumentation are described in Sections 3 and 4.

SELMA uses a unique combination of remote sensing via ultraviolet and infrared wavelengths and energetic neutral atom imaging, as well as in situ measurements of exospheric gas, plasma and dust to investigate the complex interaction of surface–space environments. Uniqueness of the SELMA mission is coordination of science and instrumentation throughout the mission; i.e., the mission design, system and instrument development, science operation, and data exploitation. Previous lunar missions have addressed only a part of the interaction. For example, the LADEE mission focused exosphere and dust, Kaguya was for surface and plasma, ARTEMIS is for plasma, and LRO is for surface and exosphere. LCROSS did an impact experiment into a permanently shadowed region, but characterization of the produced plume relied on remote sensing instruments. The SELMA mission is the first mission to investigate the interaction between the surface, exosphere, plasma and dust, using the coordinated measurements.

2. SELMA science questions

Of the very complex lunar environment interactions, SELMA focuses on four main subjects: water, volatiles cycle, mini-magnetospheres, and dust. The four SELMA key science questions can be described as follows.

1. What is the origin of water on the Moon?

The surface of non-icy airless bodes is covered with regolith, a layer of loose, heterogeneous material including dust, broken rock, and other related materials (e.g. Heiken et al., 1991). The regolith has been formed by the impact of large and small meteoroids and the steady bombardment of micrometeoroids, which slowly break down surface rocks. One of the most important manifestations of the interaction of the lunar regolith with the solar wind plasma is the formation of OH/H_2O bearing materials in the outermost layer via chemical reactions between oxygen in the regolith's minerals and implanted protons from the solar wind (Pieters et al. 2009; Sunshine et al. 2009; Clark, 2009). The solar wind protons can thus be considered as a one of the sources of water on airless bodies. On the other hand, comets may also have brought substantial amounts of water to planetary bodies during the long period of bombardment, which is another important potential source of water. Answering the question "What is the origin of water on the Moon?" is a key to understanding the water distribution and presence in the Solar System.

2. How do the volatile cycles on the Moon work?

The volatiles surrounding airless bodies form a collisionless gas layer, a surface-bounded exosphere (e.g. Stern, 1999). At the Moon, the exospheric atoms and molecules originate from the interior, and are kicked off from the regolith grain surface by solar photons and particles, and through micrometeoroids impacts. The release processes are highly variable due to the variability of the solar radiation, impinging particle fluxes, meteoroid fluxes and impact rates, surface mineralogy, temperature, topography and structures, as well as the transient releases of gas from the lunar interior. The exospheric particles do not interact with each other but with the surface and can be redistributed over the whole body. Exospheric particles originating in the hot equatorial regions may get transported to and trapped in the cold polar regions, forming volatile reservoirs there (Watson et al., 1961). Some atoms and molecules, especially those of low mass, escape to space due to sufficiently high velocities. Volatiles may also undergo ionization by solar UV radiation, and will be picked-up by the solar wind electric field, and escape the system. Answering the question "How do the volatiles cycles work on the Moon?" will reveal the sources and sinks as well as transport processes of the volatiles on airless bodies.

3. How do the lunar mini-magnetospheres work?

The Moon does not possess a global magnetic dipole field but only local crustal magnetic fields, so-called magnetic anomalies, with field strength of a few 100 s nT at the surface (e.g. Coleman et al., 1972; Richmond and Hood, 2008; Tsunakawa et al., 2015). This field strength is comparable with the weak magnetic dipole field of the Mercury (~195 nT on the equator; e.g. Ness et al., 1974; Anderson et al., 2011). The magnetic anomalies do affect the local solar wind plasma flow but cannot fully prevent it from reaching the surface (Vorburger et al., 2012). Due to the small size of the anomalies, which is between the proton gyroradius and the electron gyroradius, the electrodynamical interaction is inherently kinetic and very complex, being one of the fundamental solar wind interactions in the solar system. These lunar mini-magnetospheres are natural laboratories for studying small-scale plasma interactions in the solar system and the physics of dusty plasma. SELMA will focus on answering the question "How do the lunar mini-magnetospheres work?"

4. What is the influence of dust on the lunar environment and surface?

Levitating lunar dust, inferred from the Apollo images of horizontal glow (e.g. McCoy and Criswell, 1974; Rennilson and Criswell, 1974), fascinated scientists, and worried and bewildered engineers and astronauts. Dust was identified as the *number-one* environmental problem on

the Moon. However, the physical processes responsible for the mobilization of lofting of the dust particles are not yet fully understood due to complex interaction between the lunar surface and its UV and plasma environment. For example, the continuous interplanetary meteoroid bombardment sustains a permanently present the dust cloud in the exosphere. In addition, the plasma and associated electric fields in the exosphere control the dynamics of the dust particles. Similar processes occur at many astrophysical objects, where dusty plasmas appear frequently; for example, in interstellar molecular clouds, in proto-planetary disks, in cometary tails, planetary rings and surfaces of airless planetary bodies. Therefore, the Moon provides an exceptional testing ground for fundamental research of the physics of complex dusty plasma. SELMA will focus on answering the question "What is the influence of dust on the lunar environment and surface?"

From these four overarching science questions, we further derive several science objectives in the following sections. Table 1 summarizes the SELMA science objectives.

2.1. What is the origin of water on the Moon?

The existence of water on the lunar surface was debated for half a century. Watson et al. (1961) contested the previously common assumption that the Moon was completely dry. They considered the possibility of water in its frozen form being accumulated in permanently shadowed regions (cold traps) and calculated very low evaporation rates of ice, concluding that the cold traps should be able to retain water on geological timescales. A long series of theoretical studies were thereafter conducted, adding various possible source and loss mechanisms, with differing conclusions (e.g., Arnold, 1979; Lanzerotti et al., 1981; Hodges and Richard, 2002; Cocks et al., 2002; Crider and Vondrak, 2003).

Recent missions established that the lunar soil contains hydrogen-rich materials although the exact chemical composition ($H/OH/H_2O$, ice) is not known. The neutron spectrometer onboard Lunar Prospector (LP) observed a depletion of epithermal neutrons in the polar regions, which was interpreted as the presence of hydrogen-rich materials in the form of water inside the permanently shadowed areas (Feldman et al., 1998). The neutron spectrometer on Lunar Reconnaissance Orbiter (LRO) showed that depletions of the epithermal neutrons do not always coincide with the permanently shadowed regions but may also occur in illuminated craters too (Mitrofanov et al., 2010). Spectroscopic observations in the near-infrared (NIR) range of the OH/H_2O absorption band (2.7–3.3 μm) on the lunar surface conducted by M3 (Moon Mineral Mapper) onboard Chandrayaan-1 showed that water ice and/or hydroxyl exist in the lunar regolith (Pieters et al., 2009, Fig. 1). Similar features in the infrared spectra were found in the data from Cassini VIMS (Clark, 2009) and HRI-IR spectrometer on Deep Impact (Sunshine et al., 2009). Phobos and Deimos also exhibit similar signatures in the NIR absorption band (e.g. Fraeman et al., 2014).

Currently, two main hypotheses on the origin of OH/H_2O bearing materials are under consideration: (a) the water and hydroxyl result from chemical reactions between oxides in the lunar soil and protons implanted by the solar wind (Crider and Vondrak, 2000), and (b) the water was/is being brought to the Moon by comets, asteroids and meteoroids (Ong et al., 2010; Bruck Syal and Schultz, 2015). New evidence from LADEE is consistent with meteoritic delivery of water to the Moon (Benna et al., 2015). The key question is *"what is the role of the solar wind in the formation of the water bearing materials?"* Understanding source, accumulation and loss mechanisms for lunar water are of fundamental importance for general planetology as well as the physics and chemistry of surface-space-volatiles interactions.

In addition to the local source, there are discussions on the water vapor transport from the equatorial regions to the polar cold traps via the exosphere (Hodges 1991; Crider and Vondrak, 2002). The key question is *"how do exospheric gases affect the abundance of water bearing materials and vice versa?"*

The distribution of hydrogen-bearing materials inferred from the neutron spectrometer measurements differs from the one imaged by M3 in NIR (3 μm) band-depth (linked to OH/H_2O abundance). The signal observed by the neutron spectrometer comes from about the first meter below the surface, whereas the NIR measurement is from the top

Table 1
Science objectives of SELMA broken down from the four overarching science questions.

What is the origin of water on the Moon?
Understand the role of the solar wind in the formation of water bearing materials.
Investigate how exospheric gases affect the abundances of water bearing materials and *vice versa.*
Investigate how variable the abundances of OH/H_2O bearing materials are and how the variability is related to the plasma and neutral gas environment.
Investigate the solar wind proton balance in the lunar soil.
Determine the water content in the regolith of permanently shadowed regions and its isotope composition.
How do the volatile cycles on the Moon work?
Fully characterize the lunar exosphere.
Investigate how the lunar exospheric composition is related to surface illumination conditions and sources due to photon and thermal desorptions.
Investigate how the lunar exosphere composition is related to the plasma environment and sources due to surface sputtering.
Investigate how the lunar exosphere composition is related to impact events and sources due to impact vaporization.
Establish the sinks of the lunar exosphere.
How do the lunar mini-magnetospheres work?
Establish the structure and topology of the magnetic field at the surface.
Establish the mechanisms creating small-scale plasma depletions and deceleration of electrons and ions.
Investigate how small scale magnetic structures affect the solar wind on the global scale.
Investigate how the properties of mini-magnetospheres vary with solar wind conditions.
Investigate long-term local effects of magnetic anomalies on the surface.
What is the influence of dust on the lunar environment and surface?
Fully characterize the lunar dust environment.
Investigate how the impact events affect the lunar dust environments.
Investigate how plasma effects result in lofting the lunar plasma.

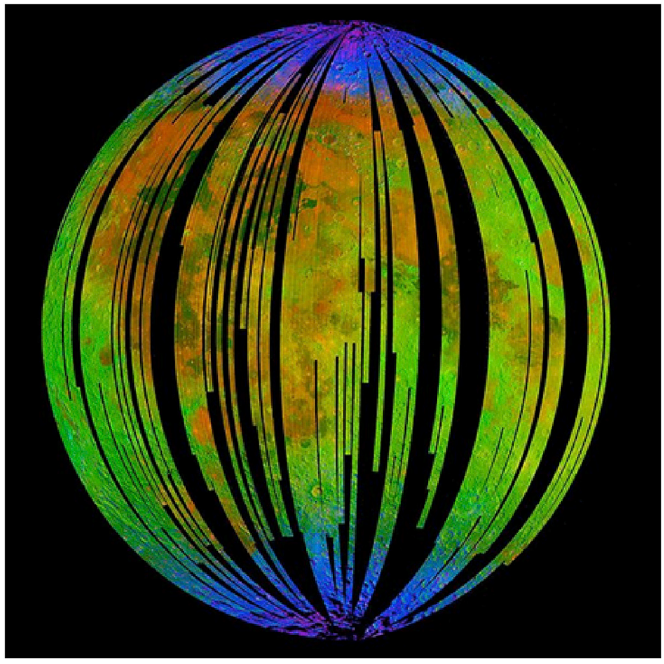

Fig. 1. Three-color composite image of reflected near-infrared radiation from the Sun as obtained by M3. Blue shows the signature of water and hydroxyl molecules as seen by a highly diagnostic absorption of infrared light with a wavelength of 3 μm. Green shows the brightness of the surface as measured by reflected infrared radiation from the Sun with a wavelength of 2.4-μm, and red shows an iron-bearing mineral called pyroxene, detected by absorption of infrared light at 2.0-μm. The figure is from Pieters et al. (2009).

micrometers of a grain. That implies that the M3 detection of OH/H_2O species is distinctly surface-correlated, i.e., linked to the upper few micrometers of the lunar regolith, but not significantly deeper. The above mentioned infrared studies showed evidence of OH/H_2O at non-permanently shadowed regions, and even at lower latitudes, seemingly more correlated to surface temperature, with daily variations (McCord et al., 2011; Li and Milliken, 2017). This result is controversial since theoretical studies were struggling to explain water accumulated in cold traps over long time-scales, whereas these observations indicated a much more rapid and transient process. While it was pointed out that the infrared observations were highly uncertain at lower latitudes (higher temperature, increasing thermal emission) and could be an instrumental effect (Clark, 2009), the high temporal variability and shallow deposits strongly suggest that solar wind impact plays a key role in water formation on the Moon. FUV observations from Lyman Alpha Mapping Project (LAMP) corroborate the diurnal variability of surface hydration (Hendrix et al., 2012). The key question is *"how variable are the abundances of the OH/H_2O bearing materials and how is the variability related to the plasma and neutral gas environment?"*

Because the hydrogen at the lunar surface should be saturated (and result in an equilibrium state between implantation into the grain and loss by diffusion from the grain), the solar wind protons are implanted in several molecular layers into grain surfaces (Lord, 1968) or diffuse to the exosphere, escaping to space in a form of atomic neutral H (Hodges, 2011) or molecular hydrogen (Hurley et al., 2017), or being trapped in the permanently shadowed regions as H_2O (Crider and Vondrak, 2000). The balance of hydrogen near the surface has been revealed to be highly controversial against that of laboratory experiments. A high amount of hydrogen is scattered back directly from the lunar surface in contrast to the lab experiments and numerical simulations. Approximately 20% of the solar wind protons are reflected back to space as neutrals with energy >30 eV (Wieser et al., 2009a; Futaana et al., 2012; Vorburger et al., 2013), 10–50% as H_2 molecules (Hurley et al., 2017) and ~0.1–1% as positively charged ions (Lue et al., 2014). Theoretical and numerical interaction models between plasma and lunar regolith, from the solar wind to the final fate, have not yet been established. The key question is *"how does the solar wind hydrogen interact with the lunar soil?"*

The LCROSS mission investigated the plume caused by the impact of an upper stage rocket into the Cabeus crater close to the lunar South Pole, and observed the water absorption line in the infrared spectrum as well as an ultraviolet emission from hydroxyl radicals, indicating a mass fraction of water in the ejected regolith of 5.6 ± 2.9% (Colaprete et al., 2010). The neutron spectrometer on LRO indicated 0.5–4.0% water ice by weight near the LCROSS impact point (Cabeus), while the water signatures spread to the sunlit region in the vicinity of the crater (Mitrofanov et al., 2010). The LAMP ultraviolet spectrograph on LRO indicated the presence of about 1–2% water in the permanently shadowed Haworth crater, yet not in the equally shadowed Shoemaker crater, situated just next to it (Gladstone et al., 2012). Reported different detections of water ice in different experiments could relate to the depth of the water ice depth. Lunar dusts at the Polar regions could cover the water ice, changing its depth structure. The key question is *"how much is the water buried in the soil of the permanently shadowed region and what is its isotope composition?"*

2.1.1. SELMA measurements (water)

In order to quantify the solar wind contribution to formation of water bearing materials on the lunar surface, global characterization of the solar wind proton flux at the surface (not at the spacecraft) together with coordinated measurements of the abundance of water bearing materials at surface will be conducted. To differentiate the source of water (solar wind origin or micrometeoroid/cometary origin), a monitoring of dust exosphere (see also Section 2.4) and impact flash measurements is conducted simultaneously. The synthetic, coordinated measurements of in situ and remote sensing measurements are the unique point of SELMA. Isotope composition, in particular for D/H ratio provides direct information on the source of the water at the surface. In addition, thorough measurements at the permanently shadowed regions are conducted to understand if and how the solar wind has direct access to these regions. SELMA undergoes an impact experiment at the end of the mission. An artificial impact into a permanently shadowed region produces a vapor plume and the density and isotope composition of the vapor are made. The information will directly address the source of the water in the cold trap. In addition, the exosphere effects on water bearing minerals are characterized. For this, exospheric gas composition and water-bearing material mapping are correlated. The influences of temporal variations of the environment (both plasma and neutral exosphere) on water bearing-materials are investigated. Long-term correlations between plasma, neutrals, and water-bearing materials at the surface are then taken. Repeated measurements in the Earth's magnetotail (~6 days every one Moon day) help to study the long-term correlations because the solar wind plasma is absent inside the magnetosphere.

Overall, these scientific investigations call for the following measurements: Coordinated mappings of the water-bearing minerals (in IR and UV range, like Pieters et al., 2009 and Gladstone et al., 2012) and solar wind flux at the lunar surface (Futaana et al., 2012). The spatial resolution of 5 km (typical crater size) for optical (IR and UV) measurements, and that of ~10 km (typical ion gyro radius) for ENA is desired. In addition, environment monitoring is of importance, namely, recordings of upstream solar wind flux (at the spacecraft), the exospheric composition and density, as well as context imaging in the visible range. SELMA further investigates the surface processes and the hydrogen balance by characterizing the scattered hydrogen species in all charge states. Fluxes of H^+, H^-, and the neutral H flying from the lunar surface are thus required to be measured. The measurement of the isotope ratios in the exospheric gas and in the impact plume are also a key.

These measurements entail the following instrumentations.

- Spectral imaging in the IR (hydroxyl and water absorption features in the wavelength range 0.4–3.6 μm) and UV (Lyman-α (121.567 nm) and water features (130–190 nm)) with spatial resolution <5 km.
- Energetic neutral hydrogen flux in the energy range 10s–a few keV with angular resolution of 5°.
- Solar wind proton (0.1–10 keV) with 30% accuracy of density and velocity.
- High mass resolution ($M/\Delta M > 1000$) mass spectroscopy of exospheric gasses to determine the isotope ratio.
- Visible camera with FoV 60° × 30° to monitor the impact flash.
- Dust monitoring to estimate the incoming micrometeoroid flux.
- Hydrogen flux in the energy range a few eV–a few keV for all the charge states separated.

In addition, the following instrumentations for the impact experiment are requested.

- A mass of 10 kg projectile, with mass spectrometer ($M/\Delta M > 1000$) flying through the plume.
- Context imaging in the visible range during the impact with spatial resolution <100 m.

2.2. How do the volatile cycles on the Moon work?

The lunar exosphere is a key region to understand the water (volatile) cycle at the Moon. Transport of gases within the exosphere is central to the lifecycle of lunar volatiles: it connects the production of volatiles at the surface (by solar wind impact or release by micrometeoroid bombardment), and their sink (photolysis, escape to space or transport to poles). The LADEE, LRO, and ARTEMIS missions have greatly advanced our understanding of the composition and structure of the tenuous lunar exosphere, yet key exospheric constituents such as water and OH remain poorly understood more than forty years after the first Apollo landing.

Very low number densities for the lunar exosphere (Fig. 2) make the

observations difficult. The multiplicity of the mechanisms responsible for the input and loss of species in the exosphere presents modeling challenges. These mechanisms include ion sputtering, photon stimulated desorption (PSD) and micro-meteoroid impact vaporization resulting in inputs to the exosphere, as well as photo-ionization, surface adsorption and escape to space from the lunar gravity field (e.g. Stern, 1999; Wurz et al., 2007, 2012).

Post-Apollo experimental work focused on the neutral sodium (Na) and potassium (K) components of the lunar exosphere, as these can be relatively easily studied from the Earth by telescopes (Potter and Morgan, 1988, 1998; Flynn and Mendillo, 1993). The behavior of Na and K is, however, not representative for most of the other species because these two elements are mostly influenced by meteoritic influx and photon-induced desorption (Sprague et al., 1992; Wurz et al., 2007).

The composition of noble gases in the lunar exosphere, measured by the Apollo Lunar Atmospheric Composition Experiment (LACE) experiment and additionally inferred from studies of gas trapped in lunar regolith samples brought to Earth indicated that species such as helium (He) are dominated by a solar wind source, but with additional contributions probably from the interior of the Moon (Hodges Jr. and Hoffman, 1975; Wieler et al., 1996). Both LADEE and LAMP observations confirm the solar wind source; they are halted when the Moon is in Earth's magnetotail (Feldman et al., 2012; Cook and Stern, 2014; Hurley et al., 2016; Grava et al., 2016). Because the solar wind impinges on the lunar surface with energies of about 1 keV/nuc H, He and other solar wind species are absorbed in the surface material (in the regolith grains and rocks) and are trapped. A fraction of the noble gases is subsequently released to become part of the lunar exosphere (e.g., Hinton and Taeusch, 1964; Johnson, 1971; Hodges et al., 1973).

The flux of heavier, more refractory, elements to the lunar exosphere is dominated by ion sputtering and micrometeoroid impact vaporization (Wurz et al., 2007). In this case, the lunar surface material will be the primary source reservoir for elements in the lunar exosphere such as Si, Ti, Al, Fe, Mg, Ca, and O, of which only O has been observed directly (Cook et al., 2013; Vorburger et al., 2014). However, pickup ions of refractory elements of lunar origin have been identified in the solar wind (Kirsch et al., 1998; Mall et al., 1998). Based on modeling (Wurz et al., 2007), the expected densities of several key elements remain several orders of magnitude lower than present upper limits.

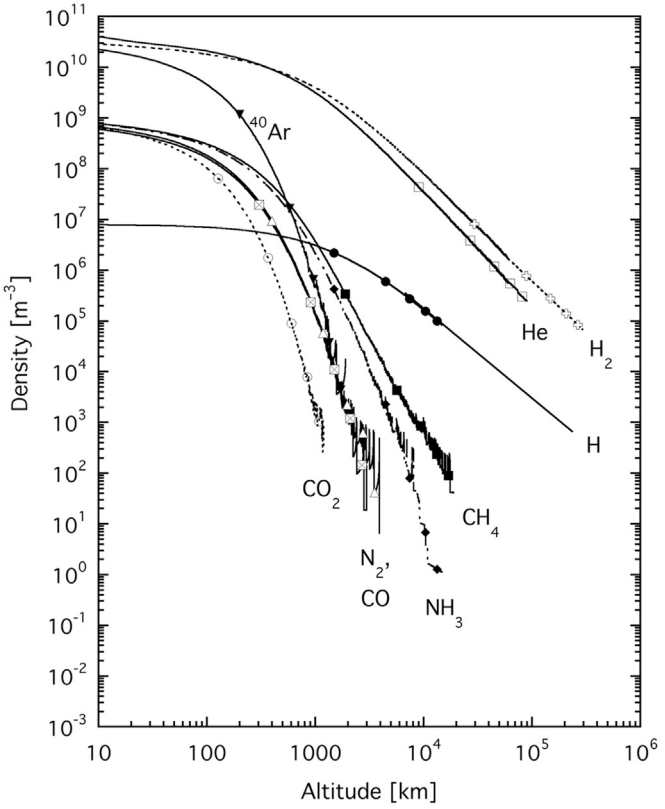

Fig. 2. Density profiles in the lunar exosphere for volatile species on the dayside (at a surface temperature of 400 K) based on measurements or upper limits (Heiken et al., 1991; Stern, 1999; Killen and Ip, 1999). Figure is from Wurz et al. (2012).

Recent measurement by LADEE has identified several neutral species in the exosphere (Benna et al., 2015), as well as ionized species (Halekas et al., 2015). Neutral He contents are controlled by the solar wind alpha particle supply in addition to rather constant endogenous source, i.e., radioactive decay from the lunar interior (Benna et al., 2015). Ne was discovered over the nightside. A localized enhancement of Ar at a specific selenographical region has also been reported (Benna et al., 2015).

Species detected in the lunar exosphere are the volatile species CH_4 (Hodges, 2016), N_2, CO_2, He, NH_3, H_2 (Stern et al., 2013), Ne, and Ar. Ionized species, H_2^+, He^+, C^+, O^+, Na^+, Al^+, Si^+, K^+, Ar^+, Ca^+ and Fe^+, have also been detected (Halekas et al., 2013), providing proof of the existence of the neutral counterpart in the exosphere (Hartle and Killen, 2006). Their densities sum up to a total density of about $2{\cdot}10^5$ cm^{-3} at the surface (Wurz et al., 2012; Stern, 1999). In contrast, from the observation of the large electron content in the lunar ionosphere, which is still debated (Imamura et al., 2010), one would infer the total neutral density to be at least a factor 10 higher (Stern et al., 2013). Alternatively, it has recently been suggested that the dust in the lunar exosphere (Horányi et al., 2015) might be the source of these electrons (Stubbs et al., 2011; Szalay and Horányi, 2015). The lack of measurement in the high-latitude regions during the LADEE mission and the earlier Apollo missions makes it difficult to discuss the localized internal source of neutrals. A global exospheric density mapping will be needed. The SELMA mission will *"fully characterize the lunar exosphere"*.

The exospheric populations at any moment are given by the strength of the release compared to the loss processes for each species and the population of the species in the lunar exosphere shows temporal variability. The transport cycle in the whole system contributes to the variability. Looking locally, the exospheric composition is determined through balances of atoms and molecules being released from the surface, which can be lost through their escape from the lunar gravity field or transported back to the surface.

Some of the release processes are driven by the Sun, i.e., the thermal release (Stern, 1999), photon dissociation desorption, and solar wind sputtering (Hinton and Taeusch, 1964). These mechanisms will introduce clear daily variations in the lunar exosphere (Hodges and Johnson, 1968). For example, He and Ne follow the exospheric equilibrium for non-condensable gasses with surface temperature (Benna et al., 2015; Hurley et al., 2016). The contribution of each mechanism to the source of the exosphere has not been identified. Although the solar conditions (photon flux, heat flux) are rather constant, unique opportunities can happen during lunar eclipses (Mendillo and Baumgardner, 1995; Potter and Morgan, 1998). The key question here is *"how is the lunar exospheric content related to the surface illumination conditions and sources due to photon desorption?"*

Because of the variable conditions in the solar wind and the existence of the Earth's magnetotail, where the Moon spends 25% of its time near the full moon period, the exosphere has also shorter time-scale variation than a lunar day. Inside the magnetosphere, where no solar wind plasma precipitates, one can expect a change of the plasma production mechanism (Wilson et al., 2006), resulting in a change of the exospheric composition. The exospheric He contents was found to follow the solar wind variation, with an assumption of 4.5-day thermal desorption time constant (Benna et al., 2015). The global characteristics change with the upstream conditions, which address the source and loss mechanisms for the exosphere as a whole, and thus for each species. The key question is *"how is the lunar exosphere content related to the plasma environment and*

sources due to surface sputtering?"

Micrometeoroids are another potential source of the lunar exosphere. Such impacts were scientifically first identified only in 1999 as pinpoint flashes (Bellot Rubio et al., 2000). The inflow flux is homogeneous over the surface and will thus add a constant influx of material to the lunar exosphere. Enhancement of the influx during meteor showers will cause a temporal increase in the exosphere of some species (Hunten et al., 1998) as well as the occasional impact of a larger meteoroid on the surface will be observable directly (Mangano et al., 2007). Recently, Neutral Mass Spectrometer (NMS) on board LADEE spacecraft examined the exospheric species changes resulting from Chang'E 3's landing on 14 December 2013. No large effects on the exosphere by the exhaust materials were detected (Elphic et al., 2014). This could be due to the long time difference and the distance between the measurement place and the landing side (after 30 min, LADEE passed the nearest point to the landing site with a separation of 1300 km). In addition, the three primary constituents of the exhaust plume fall in mass channels that have high instrumental background levels. The spatial and temporal variations in the exospheric characteristics are the key to understand its circulation. Therefore, the key question here is *"how is the lunar exosphere content related to impact events and sources due to impact vaporization?"*

The exospheric particles will be lost from the system on specific time scales. Loss mechanisms include surface adsorption or attachment (including those in the cold trap), and escape to space (including direct escape, thermal (Jeans) escape, and via the photo-ionization). Surface attachment is directly associated to the reservoir of volatiles, in particular for the cold traps. The direct escape (when the particles have more speed than the escape speed of 2.4 km/s, on their generation) depends on the source mechanisms. Ion sputtering or scattering may result in direct escape for lighter particles (Thompson, 1968; Wurz et al., 2007), but the photon-stimulated desorption or thermal desorption can hardly produce such high energy particles. The thermal escape might work only for lighter species such like hydrogen or helium (Killen et al., 2017). For most of the heavier particles, the escaping mechanism is via the photo-ionization. The SELMA mission aims to understand *"the sinks of the lunar exosphere."*

2.2.1. SELMA measurements (exosphere)

A full characterization of the lunar exosphere will be conducted by the determination of its composition. The composition will be surveyed globally, including the polar regions. Global maps, as well as the altitude profiles of 30–200 km, of the abundances of all main components (H, H_2, He, O, OH, Ne, Na, Ar, K, Ca, CH_4, N_2, CO, CO_2, NH_3, Kr, Xe) are produced. To separate the isotope ratio of the order of 10^{-4} between $_{16}O$ and $_{17}O$ (in the solar system; Yurimoto et al., 2007), M/ΔM>1000 is desired. The investigation of the solar-photon induced exospheric composition will be addressed by measurements of the temporal (daily to monthly) variability of the lunar exospheric compositions. Indeed, a unique opportunity occurs during the lunar eclipses, when the flux of solar photons is completely shut off owing to Earth's shadow. Another temporal variation of the exosphere could be induced by the plasma, depending on where the Moon is located (in the solar wind or in the Earth's magnetosphere). To evaluate the plasma contribution to the exospheric content, the correlation between the variations in local plasma conditions and the exospheric characteristics is investigated by coordinated measurements of the plasma and exospheric gas. To quantify the composition of the plasma, separation of K^+ and Ca^+ is aimed (Yokota and Saito, 2005), corresponding to M/ΔM~80. To investigate impact vaporization as a source of the exospheric material, the correlation between lunar exosphere variations and impact events is explored. Thus, impact events should be measured together with the exospheric gas density. The sink for exospheric species is investigated by measuring escaping particles. The fluxes of the escaping ions (non-thermal) and neutrals (thermal) are quantified to derive the escaping flux from the exosphere to space. Measuring the exospheric ions and neutral species in a wide altitude range is a key measurement for this investigation.

These measurements ask for the following key instrument characteristics.

- Continuous measurements at high mass resolution (M/ΔM>500) of the composition of exospheric gasses.
- Ion and electron fluxes in the energy range of 10 s eV–a few keV.
- Ion mass composition (M/ΔM > 80) from the Moon in the energy range of 10 eV–20 keV with moderate (25%) energy resolution.
- Measurements of light flashes from 100 g meteoroids.

2.3. How do the lunar mini-magnetospheres work?

The Moon currently does not have a global dipolar magnetic field, as would be generated by a liquid metal core dynamo. However, the Moon has localized crustal magnetizations of up to a few 100 nT called magnetic anomalies. These anomalies, first discovered by Apollo 12 (Dyal et al., 1970), are spread over the whole surface, mostly clustered on the lunar far side (Richmond and Hood, 2008). They were probably formed early in lunar history when the dynamo was still operating (Purucker et al., 2012). Alternatively, some of the remnant magnetization may be from transient magnetic fields generated during large impact events, through the expansion of an impact-generated plasma cloud in the presence of an ambient magnetic field. This is supported by the apparent location of the largest magnetic anomalies near the antipodes of the giant impact basins (Hood and Huang, 1991; Wieczorek et al., 2012).

The interaction of the magnetic anomalies with the solar wind is of special interest for plasma physics, because it occurs over multiple scales, namely from the fluid scale (plasma can be described as a fluid, on scales larger than the ion scale, >100 km) to the electron scale (electron kinetics are important, <100 m). The effects of magnetic anomalies on the solar wind were detected during the Apollo era as an increase of the solar wind magnetic field caused by the increase of the solar wind density above the anomalies (Russell and Lichtenstein, 1975). Although some numerical studies have been conducted, due to the very small scale (altitude scale is ~10 km, which is significantly smaller than the ion scale in the solar wind) and lack of lunar missions for long time after Apollo, no detailed studies had been conducted until 1990s. Electron and magnetic field data from Lunar Prospector over an area of clustered magnetic anomalies at the Imbrium antipode, indicatively showed signatures of a bow shock (Lin et al., 1998) and plasma void (Halekas et al., 2008). It was concluded that a mini-magnetosphere was formed. Such mini-magnetosphere reduces the flux of the solar wind precipitation on the lunar surface as shown in Fig. 3 (Wieser et al., 2010; Vorburger et al., 2012; Futaana et al., 2013). The formation, structure and characteristics of the mini-magnetosphere are dominantly controlled by the magnetic field orientation (Deca et al., 2015; Fatemi et al., 2015). In particular, due to the lack of the measurement of magnetic field at the surface, we do not know whether the horizontal field plays a more important role than the vertical field (Wang et al., 2013) or vice-versa (Poppe et al., 2016). Overall, the interaction between the magnetic anomaly and the solar wind is highly controlled by the magnetic field geometry. SELMA aims at establishing *"the structure and topology of the magnetic field at the surface."*

Near the magnetic anomaly (and most likely inside the mini-magnetosphere), Lunar Prospector observed increases in low-energy (<100 eV) electron fluxes simultaneously with large magnetic field amplifications, which is consistent with an increase in plasma density across a shock surface. Low frequency wave activity in the magnetic field data (both broadband turbulence and monochromatic waves) was often associated with electron energization, sometimes up to keV energies.

Due to the small size of the magnetic anomalies, the mechanism deflecting the solar wind is not well understood (Kallio et al., 2012). Likely, the protons are affected by the ambipolar electric field, which is set-up by the charge separation between magnetized electrons and non-magnetized protons (Saito et al., 2012; Futaana et al., 2013) or by the Hall electric field due to the different motions between the ions and electrons (Jarvinen et al., 2014). In addition, at the lunar surface, surface

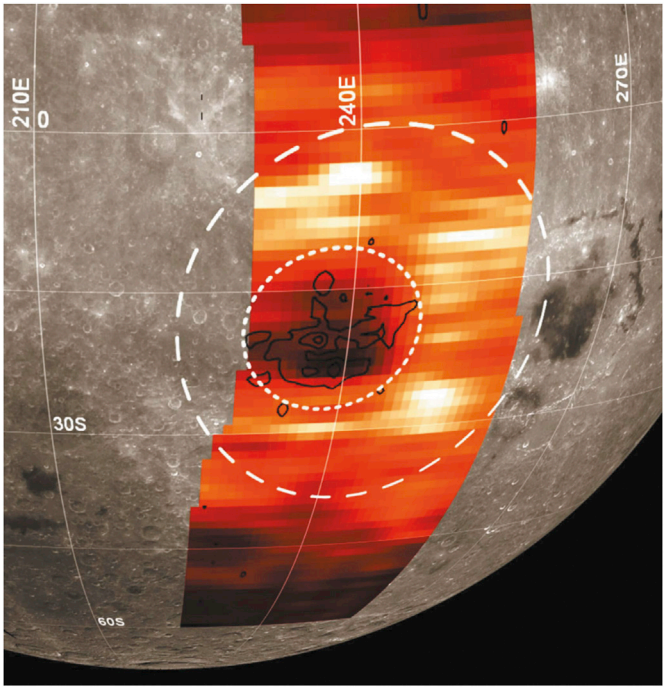

Fig. 3. Formation of mini-magnetosphere proven by energetic neutral atom measured by Chandrayaan-1/SARA instrument. The flux of the emission is proportional to the solar wind flux at the lunar surface. The magnetic anomaly influences the solar wind flux close to the surface (below the spacecraft). Figure is from Wieser et al. (2010).

potentials are formed due to the balance between plasma currents and photoelectron currents (Vondrak, 1983). The photoelectron emission from the surface also influence in the electron scale environment near the surface via an electric potential formation (Poppe et al., 2016). In summary, the electrons play significant roles in the interaction region. SELMA establishes *"the mechanisms creating small-scale plasma depletions and deceleration of the electrons and ions associated with mini-magnetospheres."*

Kaguya and Chandrayaan-1 have also conducted in situ measurements of particles and fields above the anomalies. Proton deceleration and electron heating were observed from 100 km down to few 10 s km (Saito et al., 2012). The solar wind proton flow deviation above anomalies is detectable up to 100 km altitude and occurs over large areas because the anomalies affect the solar wind in a coherent way (Lue et al., 2011). Over the strongest anomalies up to 50% of the solar wind flux is deflected. This significant flux of the deflected protons causes a change in the morphology in the interaction (Fatemi et al., 2014) by creating a large-scale disturbance of the solar wind, and trajectories that allow protons to reach the lunar wake and the nightside surface. The key question is *"how does the magnetic anomaly affect the solar wind on the global scale."*

The mini-magnetospheres associated with the anomalies show strong variability with solar wind conditions (Vorburger et al., 2012). For example, a mini-magnetosphere associated with an isolated magnetic anomaly close to the Gerasimovich crater shows clear response to the solar wind dynamic pressure. Most other magnetic anomalies (more than half) on the lunar surface have more small-scale features in their magnetic field and do not show such a clear correlation with the solar wind conditions demonstrating a very complex interaction. Lunar Prospector also observed the variability of the anomaly effects on the solar wind depending on the solar wind conditions and solar zenith angle due to the geometrical changes in the solar wind dynamical pressure. Theories and simulations support these observations (e.g. Fatemi et al., 2015; Zimmerman et al., 2015; Deca et al., 2015). The variability of the solar wind flux reaching the surface does affect the proton implantation rate. The key question is *"how do the properties of mini-magnetospheres vary with solar wind conditions?"*

It was noticed that many of the magnetic anomalies correlate in location with specific albedo features on the surface, called swirls. It was suggested that this is a manifestation of the space weathering effect (Hood et al., 2001). Recently, alternative ideas link the differences in albedo with the redistribution of lunar dust, which is charged and thus governed by magnetic and electric fields set up by the interaction between a magnetic anomaly and the solar wind (Garrick-Bethell et al., 2011). The key investigation is *"the long-term effects of magnetic anomalies on the local surface."* The alternation of the impinging solar wind pattern influences the distribution of the volatiles close to the magnetic anomaly.

2.3.1. SELMA measurements (mini-magnetosphere)

SELMA characterizes the topology of the magnetic field down to the lunar surface. All components of the magnetic field vectors are measured. To establish the small-scale plasma depletion and deceleration mechanisms, ions, electrons and, electromagnetic waves inside the mini-magnetosphere are also measured. The 3-D velocity distributions of ions and electrons (with energy 10 s eV–a few keV) are measured simultaneously with the electromagnetic waves to evaluate the dynamics of the environment. These measurements should be conducted very close to the surface down to the electron scale (~100 m). For this investigation, the high time resolution is a key: 0.05 s for fields and 0.5 s for particles. To do this, SELMA is equipped with an impact probe, SIP-MA, which will be released to the Reiner Gamma region.

On the other hand, to investigate the global impact of magnetic anomalies on the upstream solar wind characterization of the keV-energy plasma together with knowledge of the local magnetic field is requested. This should be achieved by in situ measurement of 3-D proton and electron velocity distributions and magnetic field. The solar wind impact on the mini-magnetosphere structures can be addressed by energetic neutral atom imaging (Vorburger et al., 2012) combined with in situ solar wind monitoring. This measurement requires the ENA imaging with a 10 km resolution because the typical size of the mini-magnetosphere is 100 km. Simultaneously, the solar wind parameters should be obtained. These measurements are conducted by the SELMA orbiter with its altitude coverage of 30–200 km.

The study of long-term effects of mini-magnetosphere on the lunar surface, interdisciplinary measurements are coordinated, namely, SELMA combines remote sensing in the wavelength of IR, VIS, and UV ranges together with in situ plasma measurements. Assessment of the lofting dust contribution to the changes in the swirls is also investigated. These interdisciplinary studies are enabled by systematic coordination among the impinging solar wind flux, albedo in the visible range, OH/H_2O related spectra, and local dust measurement (>0.3 μm).

These measurements entail the following key instrument characteristics for the SELMA orbiter.

- Total ion and electron fluxes in the energy range of 10 s eV–a few keV.
- Solar wind proton (0.1–10 keV) with 30% accuracy of density and velocity.
- Magnetic field vector ranging from 0.1 nT to 5000 nT with an angular accuracy <10°.
- Energetic neutral atom for the surface imaging with energy of 100 eV–3 keV, with spatial resolution <10 km at the surface.
- Visible surface image with resolution <1 km at the surface.

In addition, the impact probe instrumentations should comply with the followings.

- Magnetometer >40 Hz with accuracy of ΔB<1 nT (or ΔB/B>1%) for 1–2000 nT.
- Ion and electron spectrometer in the energy range of 10 eV–a few keV with a time resolution of 0.5s.

- Electric field measurements in the frequency range 1 MHz down to DC.

2.4. What is the influence of dust on the lunar environment and surface?

The lunar dust environment is expected to be dominated by sub-micron dust particles (Horányi et al., 2014). These particles originate from highly weathered lunar regolith. The typical grain size range is from centimeter scale to submicron scale (Heiken et al., 1991). During the Apollo era, so-called horizontal glow was unexpectedly discovered by astronauts in orbit. It is caused by scattered sunlight, appearing at the terminators (e.g. McCoy and Criswell, 1974; Rennilson and Criswell, 1974). This scattered light has been believed to be due to lofted dust, most likely ejected by strong electrostatic forces in the vicinity of the lunar terminator (Criswell, 1973; McCoy and Criswell, 1974; Rennilson and Criswell, 1974; Berg et al., 1976; Zook and McCoy, 1991). Modeling efforts suggested a significant dust exosphere (typical grain size of 0.1 μm) over the terminator region, extending to altitudes above 100 km, with an integrated column density of 10^{-10} kg/m^2. (McCoy 1976; Zook and McCoy 1991; Murphy and Vondrak, 1993). The electrostatic forces that make the dust grains lofted have been discussed (Stubbs et al., 2006 and reference there in), but no firm conclusion has been provided. Recent fully kinetic calculations show the effect of electric fields on the lunar dust populations (Dyadechkin et al., 2015; Kallio et al., 2016). One of the main difficulties in the discussions about the dust environment is the lack of the in situ measurements of dust grains.

The first attempt to observe the lunar ejecta cloud by the Munich Dust Counter on board the HITEN satellite orbiting the Moon (15 February 1992 to 10 April 1993) did not succeed, owing to its distant orbit and low sensitivity (Iglseder et al., 1996). The Lunar Dust Experiment (LDEX) onboard NASA's Lunar Atmosphere and Dust Environment Explorer (LADEE) began its measurements on 16 October 2013 and detected a total of approximately 140,000 dust hits in the altitude range of 1–250 km during about 80 days of cumulative observation time out of 184 total days by the end of the mission on 18 April 2014 (Elphic et al., 2014). LDEX was designed to explore the ejecta cloud generated by sporadic interplanetary dust impacts, including possible intermittent density enhancements during meteoroid showers, and to search for the putative regions with high densities of 0.1-μm-scale dust particles above the terminators (Horányi et al., 2014). Due to the limitation of the orbiter trajectory, only the equatorial region (±22° from the lunar equator) was explored. Therefore, SELMA will complete the emerging picture, *"fully characterizing the missing portions of the lunar dust environment."*

There are two main mechanisms for maintaining the lunar dust cloud: 1. Ejecta production by continuous bombardment of interplanetary dust particles; and 2. the putative electrostatic lofting of surface materials. The Moon is continually bombarded by interplanetary dust particles (IDPs), liberating orders of magnitude more solid ejecta than the impacting particles. Only a small fraction of the impact generated ejecta particles escape lunar gravity, and most of them follow ballistic orbits and form a gravitationally bound dust exosphere around the Moon. IDPs are delivered to the Moon at a rate of ~5000 kg/day (Grün et al. 1985). Their characteristic radius is ~100 μm with typical speeds of 20 km/s (Taylor 1996). Those ejected particles form the dust cloud (Grün et al., 2011). The lunar dust cloud was first observed by LDEX (Horányi et al., 2015, Fig. 4). Ejecta clouds were also observed by the Galileo mission during flybys of the icy moons of Jupiter: Europa, Ganymede and Callisto (Krüger et al., 2000).

Strong temporal variability of the dust density was observed by LDEX on LADEE, most likely associated with the stochastic nature of the meteoroid impacts. Moreover, intermittent density enhancements were also observed during several of the annual meteoroid streams (Horányi et al., 2015). Clear spikes in the dust impact rate during the well-known meteor shower (for example by Taurids and Geminids) were detected. On the other hand, the rendezvous of LADEE with Chang'E−3 landing (Elphic et al., 2014) did not provide any clues of dust signals. It is very unlikely to be observed because the separation between the two spacecraft was too large.

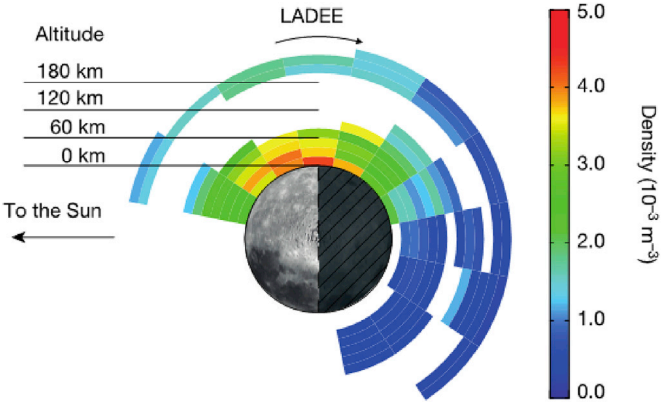

Fig. 4. The top-down view of the dust particle density (a >0.3 μm) projected onto the lunar equatorial plane. While pointed near the direction of the motion of the spacecraft, LDEX did not make measurements between 12 and 18 local time. White coloring indicates regions where LADEE did not visit or was not set up for normal operations. Figure is from Horányi et al., (2015).

Nevertheless, LDEX measurements during intense meteoroid showers indicated strong correlations with dust influx. However, the quantitative assessment between the dust cloud and the impact flux could not be fully characterized based on LDEX measurements alone. In addition, the question of what is the direct influence by a relatively large impact to the dust cloud still remains. The key question is *"how do the impact events affect the lunar dust environment?"*

Another putative source mechanism for high altitude lunar dust is electrostatic lofting. UV radiation and/or solar wind plasma near the surface is expected to induce intense electric fields near the terminator region (Sternovsky et al., 2008). The electric field may loft dust particles with characteristic radii of ~0.1 μm (McCoy and Criswell 1974; McCoy 1976). This phenomenon is preferably occurring near the terminator region, where the sunlit and shadow boundary exists. The effect of varying surface potentials because of shadowing on the lofting of lunar dust was shown in recent simulations (Dyadechkin et al., 2015). Due to the different illumination conditions, the surface potentials may differ (Vondrak, 1983), and strong electric fields are expected to exist. Due to the coincidence of the strong electric field potentials and the scattered sunlight measured by Apollo astronauts, the lofted dust particles are assumed to be responsible for the horizontal glow.

However, the processes involved remain controversial. Observations by the start tracker camera onboard the Clementine (Glenar et al., 2014) and the LAMP instrument onboard the LRO (Feldman et al. 2014) indicate the upper limits for the density of the high altitude dust exosphere lower than the previously reported densities. LDEX did not find any evidence for the expected density enhancements over the terminators (Horányi et al., 2015). Overall, no observations (other than the indirect evidence of horizontal glow) have successfully supported the existence of lofted dust. As of yet, unknown conditions or UV illumination and/or plasma exposure may be important to generate electrostatic dust lofting. The key question is *"how might plasma effects result in lofting the lunar dust?"*

2.4.1. SELMA measurements (dust)

SELMA will be the first to fully characterize the global lunar dust environment. Correlations between the variability of the global dust distribution and the exospheric profiles will be taken; the investigation is realized by simultaneous time-series measurements of dust characteristics and the exospheric composition and spatial profile. As the lunar dust environment is thought to be dominated by submicron-sized dust, the dust size distribution down to 0.3 μm is measured. To understand the origin of the lunar dust environment, correlations between impact events

(both natural bombardment of >100 g meteoroid or artificial impactor) and dust profiles are to be investigated. Simultaneous measurements of the dust size distribution and monitoring of the meteoroid impact are necessary. An artificial impactor of 10 kg would realize the measurement. The correlation of the dust population with the plasma environment will also be investigated. It is realized by characterizing the dust environment while simultaneously monitoring the plasma particle populations and electric and magnetic fields. Simultaneous measurements of the dust size distribution and plasmas observations are thus conducted.

These measurements call for the following key instrument characteristics for the SELMA orbiter.

- Dust flux >0.3 μm (>10^{16} g).
- Electric field from DC–1 MHz.
- Continuous measurement of high mass resolution (M/ΔM > 500) mass spectroscopy of exospheric gasses.
- Measurements of light flashes from 100 g meteoroids.

In addition, the following instrumentations for the impact experiment are requested.

- A mass of 10 kg projectile into a known permanently shadowed crater.
- Electron 3D distribution functions with time resolution of 0.5 s.
- Electric and magnetic field.

3. SELMA mission

3.1. SELMA mission overview

The SELMA mission is designed to achieve the SELMA science objectives (Table 1). For this purpose, the SELMA mission includes an orbiter, an impact probe SIP-MA, a passive impactor, and a simple relay CubeSat (RCS) (Table 2). The SELMA orbiter is inserted into a low maintenance quasi-frozen orbit 30 × 200 km with the pericenter over the South Pole, similar to the NASA LRO orbit. The lifetime is 15 months in order to cover all the known meteor shower events. All instruments operate throughout the whole missions (see Table 3).

Two impact experiments are conducted during the mission. The first impact experiment is at six months after the launch; the impact probe SIP-MA is released targeting the Reiner-Gamma magnetic anomaly region to address the "mini-magnetosphere" science. During the descent SIP-MA transmits the data to the SELMA orbiter. The lifetime of SIP-MA is ~30 min. The requirement is that the experiment is done when the Moon is in the solar wind, and when the solar zenith angle of the target magnetic anomaly is 40–60°. The primary target is the Reiner Gamma area (Hood et al., 1979). This required geometric constellation is realized every month. Therefore, there are no requirements of the experiment time. Here tentatively we assumed to conduct the measurement 6 months after the SELMA launch.

The second impact experiment is for the direct measurement of the water content inside the permanently shadowed region (for "water" science, as well as "exosphere" and "dust" sciences). This is conducted at the end of the mission. The target is, as a primary candidate, the Shackleton crater. The sequence is summarized in Fig. 5. Two elements are released: a passive impactor and a relay cubesat (RCS). The passive impactor targets the permanent shadowed region to make an artificial impact. Prior to the impact, the SELMA orbit is changed to a circular lunar orbit (CLO) of 400 km altitude (1) to increase the impact angle to 10°. After a few orbits, RCS, serving as a data relaying satellite during the SELMA impact, is released with a low ΔV (2). RCS closely follows SELMA in its CLO. Shortly after the RCS release, SELMA performs a ΔV-maneuver targeting a point of impact in the Shackleton crater (3). Immediately after the impact maneuver, a passive impactor is separated (4) to impact the surface >10 s ahead of SELMA to create a plume (5), which the SELMA orbiter investigates before the impact (6). The SELMA orbiter will crash to the surface in the end (7). During the descent the science data are continuously transmitted from SELMA the ground and to the RCS, still in its 400 km altitude orbit, that stores the data on-board for later downlink to Earth. RCS is required to record the data when SELMA is in the crater out of visibility from the ground and to back-up the data received during this critical operation.

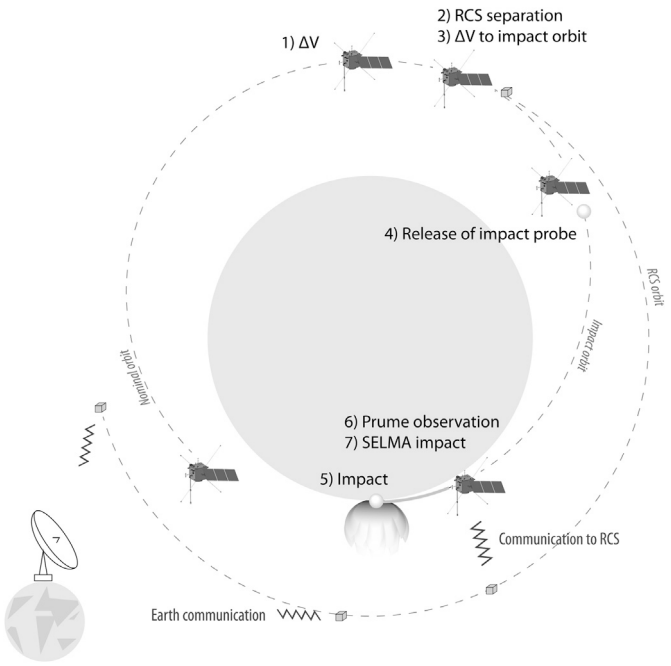

Fig. 5. Impact experiment sequence to investigate a permanently shadowed region (not in scale).

3.2. SELMA mission elements

3.2.1. SELMA orbiter

The SELMA orbiter is designed to accomplish a majority of the scientific objectives. The orbit of 30–200 km is the primary requirement; the pericenter altitude was defined from the precise imaging for "water" science as well as the in situ measurements needed for the "mini-magnetosphere" science. The pericenter latitude is at the South Pole, because of the concentrated permanently shadowed region at the South Pole, as well as the aggregation of the magnetic anomalies in the southern hemisphere. The apocenter altitude was defined to enable monitoring of the global meteoroid impacts (influencing "volatile cycles" and "dust" sciences) and to meet the need for altitude profiles of the exospheric composition (for "volatile cycles" sciences). The mission length is for 15 months, which cover one full Earth year observation so that the mission covers all meteor shower events, maximizing the opportunity of detecting impact events. The launch date is flexible.

The SELMA orbiter is a 3-axis stabilized spacecraft. The SELMA orbiter hosts four remote-sensing instruments and seven in situ instruments. These sensors are accommodated to conduct the coordinated observations; for example, the co-aligned remote-sensing sensor fields of

Table 2
SELMA mission elements and their time line and the lifetime.

Elements	Time line	Life time
SELMA orbiter	Moon orbit insertion after 4–5 days after launch	15 months
SIP-MA	Impact probe experiment 6 months after launch	30 min.
Impactor (passive)	Impact experiment 15 months after launch	30 min
RCS	Impact experiment 15 months after launch	87 min

view. All the sensors are operated continuously. Fig. 6 shows the SELMA orbiter design. Four booms are deployed for the electric field measurements, and a single boom for the magnetic field measurements.

3.2.2. SELMA Impact Probe-Magnetic Anomaly

Some of the scientific objectives for the "mini-magnetosphere" science require the very low altitude measurement (0.1 km altitude) inside a magnetic anomaly. A dedicated impact probe is thus launched from the orbiter. The impact probe, SELMA Impact Probe-Magnetic Anomaly (SIP-MA), flies through the mini-magnetosphere to measure the plasma characteristics using very high time resolution instruments. After the measurement, SIP-MA will crash into the lunar surface. The key region is below an electron gyroradius (0.1 km; 10 eV electron under 100 nT). Fig. 7 shows the SIP-MA mechanical design. Four booms for field measurements are deployed after the separation. The measurements are conducted down to the altitude range below 0.1 km. To descent from the altitude of 0.1 km to the surface to crash, SIP-MA typically takes 1–3 s (assuming 1–2° of impact angle). Thus, 3-D proton and electron distribution with full angular coverage within 0.5 s, together with DC electromagnetic fields are measured. Four in situ sensors are accommodated (see Section 4 for details).

3.2.3. Passive impactor

To produce the enough material from the permanently shadowed crater for the impact experiment, a passive impactor is prepared. It is a 10 kg copper sphere, with which Holsapple and Housen scaling law model (http://keith.aa.washington.edu/craterdata/scaling/index.htm; Housen and Holsapple, 2011) predicts ~700 kg ejecta. Assuming 6% water content in the permanently shadowed crater (Mitrofanov et al., 2010), 40 kg (2000 mol) of water molecules are released. Assuming a 10 km scale plume (~10^{18} cm^3), the density becomes of the order of

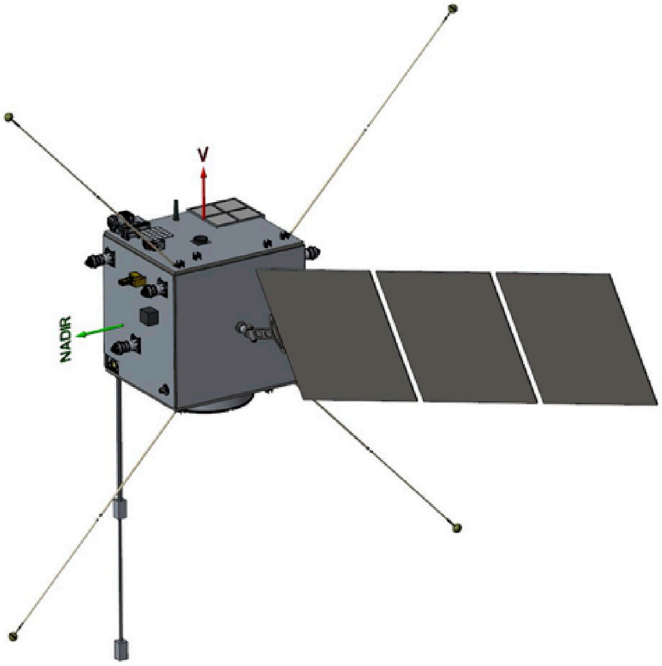

Fig. 6. SELMA orbiter design. The SELMA orbiter is a 3-axis stabilized platform, with a solar array with a 2-axis driving mechanism on one side of the bus in order to realize continuous measurements over the one Earth year (mission lifetime). The remote sensing instruments are mounted in the nadir deck (green arrow in the figure), always pointing to the lunar surface, sharing the same boresight. In situ instruments are located either the nadir deck, ram deck (red in the figure), or zenith deck (anti-nadir direction, not visible in the figure). Four long booms are for the electric field measurement (Orchestra), and another boom is for magnetometer. The block at the top-right corner is SIP-MA (See section 3.2.2). (For interpretation of the references to colour in this figure legend, the reader is referred to the web version of this article).

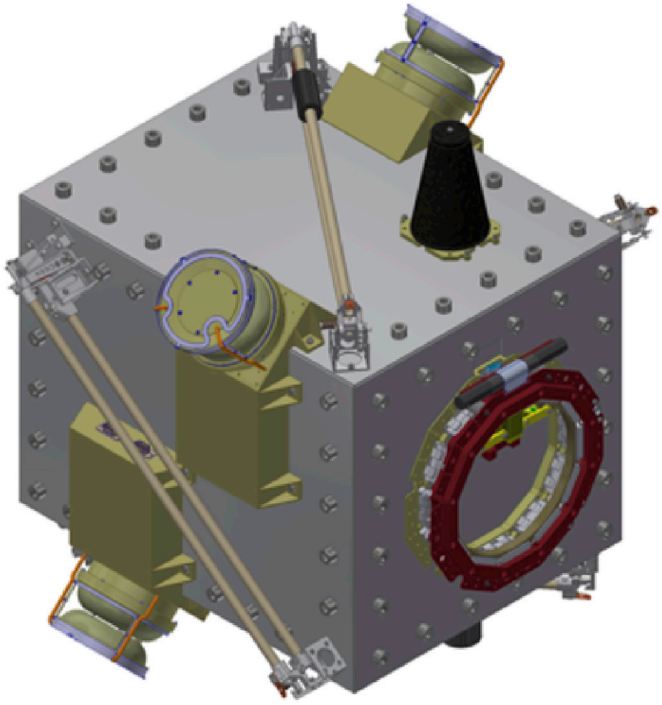

Fig. 7. SIP-MA mechanical design. Red-colored ring structure in the right is a separation ring. Four sensor heads (three are visible in this figure) are for the ion and electron spectrometers to cover 4π field of view together, and the four booms (two are visible) are deployed for electric (mini-EF) and magnetic (IPMAG) fields. (For interpretation of the references to colour in this figure legend, the reader is referred to the web version of this article).

10^9 cm^{-3}. While the water molecule content in the regolith is highly uncertain, and the assumed 6% is the highest value ever reported: a 10 kg impactor produces 10^3–10^4 times higher density of water compared to the natural exosphere (10^5–10^6 cm^{-3}). To have sufficient sampling time for the mass spectrometer inside the plume, the spacecraft has to travel through the plume for longer than10 s.

3.2.4. Relay CubeSat

A relaying cubesat, RCS, is released in order to receive the measured data by the SELMA orbiter during the last seconds. The received data will be transferred to Earth. RCS is required because the SELMA orbiter becomes invisible from Earth when it enters to the shadowed crater. RCS is a 6U cubesat, with S-band communication package and a simple camera to monitor the SELMA impact.

4. Science payload

Table 3 Summarizes the proposed science payload and their key measurements, as well as the required key performance to satisfy the SELMA science cases. Tables 4–6 show the summary of payload performance.

4.1. IR and visible spectrometer (VIS-NIR)

The IR spectrometer for SELMA is based on the heritage of the SIR-2 spectrometer (Mall et al., 2009) and the experience of the M^3 instrument on Chandrayaan-1 (Pieters et al., 2009). The spectrometer consists of an optical unit, a wedge filter (or Linear Variable Filter, LVF), a dual-hybrid detector and a thermoelectric cooler. A LVF is a band-pass filter whose coating has been intentionally wedged in one direction. Since the band-pass' center wavelength is a function of the coating thickness, the peak wavelength transmitted through the filter will vary in a linear

Table 3
SELMA science payload and the required key performance. Contributions to the science questions are also indicated by X (for major contribution) and x (for interdisciplinary contribution).

Instrument name	Full name	Key measurement	Key performance	Water	Exosphere	Mini-magnetosphere	Dust
SELMA orbiter							
VIS-NIR	IR and visible spectrometer	H_2O/OH/ice detection on the surface	Spectral range 400–3600 nm	X		X	
SPOSH	Wide angle and transient phenomena camera	Surface context imaging, transient phenomenon detection, meteoroid impact	Visible range; FoV: 120° × 60° Meteoroid mass: 10s g- 1 kg	X	X	X	X
MUVS	Moon UV imaging spectrograph	Surface UV spectroscopy	Spectral range 115–315 nm	X	X	X	
ENAT	ENA telescope	Backscattered hydrogen to monitor proton flux impinging the surface	Energy range 10 eV–3 keV. Ang. resol. < 10°	X	X	X	
LIS-SW	Lunar positive ion spectrometer	Positive SW ion distribution functions	Energy range 1 eV–10 keV 3D coverage (2π)	X	X	X	(x)
LIS-MS	Positive ion mass spectrometer	Positive ion mass composition Secondary ion mass spectroscopy	Energy range 10 eV–1 keV 3D coverage (2π) M/q > 2 M/ΔM > 50	(x)	X	X	(x)
LSHE	Lunar scattered proton and negative ions experiment	Scattered negative hydrogen and proton distribution functions Solar wind monitoring from nadir plane	Energy range 1 eV–10 keV 3D coverage (2π)	X	X	X	(x)
LES	Lunar electron spectrometer	Electron distribution functions	Energy range 1 eV–10 keV 3-D coverage (4π) Time resolution 1 s		X	X	X
MMAG	Moon Magnetometer	Magnetic field vector	0.1–30000 nT ΔB < 0.1 nT			X	X
LEMS	Lunar Exospheric Mass Spectrometer	Exosphere composition and content	M/ΔM > 1000	X	X		X
Orchestra	Plasma Wave Instrument	Plasma waves and electric field	Sampling frequency 10 kHz ΔE< 1 mV/m	X			X
LDD	Lunar Dust Detector	Dust size, fluxes, and velocities	Dust particle mass down to 10^{-16} kg				X
SIP-MA							
MiniEF	Waves and electric field	Electric field measurement	Frequency 1.4 MHz Spatial resolution 100 m			X	X
IPEI	Impact probe ions and electrons spectrometer	Ion and electron distribution functions	Energy range: a few eV–a few keV Time resolution: 0.5s/3D 3D coverage (4π)			X	
IPMAG	Impact probe magnetometer	Magnetic field vector	Range: 0.1–30000 nT ΔB < 0.1 nT			X	
IPCAM	Context camera	Context imaging PR imaging	Video stream			X	
Impact experiment							
Passive impactor (*)		Passive impactor	10 kg	X	X		X
IECAM	Context camera	Context imaging PR imaging	Video stream	X			

Table 4
SELMA orbiter remote sensing instrument performances.

Instrument	VIS-NIR	SPOSH	MUVS	ENAT
Objective	Photon	Photon	Photon	ENA
Spectral range	400–3600 nm	400–800 nm	115–315 nm	
Spectral resolution	λ/dλ = 100		1.2 nm	
Field of view	3.2°	61.7°	0.3 × 7.5°	10 × 10°
Angular resolution	0.015°	0.031°	0.06°	5 × 5°
Sampling time	<6 ms			0.5s
Energy range				10 eV–3 keV
Energy resolution				50%
Mass range				1–70 amu
Mass resolution				H and heavies

fashion in the direction of the wedge. The LVF has at a given point a Gaussian transmission profile, at which radiation is transmitted. The LVF has a range between 0.4 and 3.6 μm over a length of approximately 10 mm. The filter is mounted on a substrate, which exactly fits the detector. The dual-hybrid detector (silicon for pixels 1–70 and HgCdTe for pixels 71–280) is thermally insulated and is cooled and stabilized through a four-stage Peltier element. The option with a radiator similar to the Chandrayaan-1/SIR-2 is also available and used for the spacecraft mechanical layout. The spectral dispersion is achieved only through the LVF. The optics have a focal length of 150 mm and an f-number of 4.5 yielding an IFOV of 0.015° per pixel which corresponds to a ground-sampling distance of 20 m/pixel at an altitude of 100 km. At a spin rate of 1 rpm, the resulting dwell time for one IFOV will be around 6 ms. The active FOV is 3.2° × 3.2°.

4.2. Wide angle and transient phenomena camera (SPOSH)

The SELMA wide-angle camera, based on the Smart Panoramic Sensor Head (SPOSH), is a frame camera built to observe meteoroid impacts and possible other luminous night time phenomena in the visible range (400–800 nm) on the dark hemisphere of the Moon (Oberst et al. 2011), and will allow detection of any meteoroid impact with a mass larger than a few grams. In spite of the highly sensitive CCD (1024 × 1024 pixels), we foresee limited daylight operation for context imaging. The camera contains a camera head that consists of an optical telescope with a wide-angle lens and a detector unit. The highly sensitive CCD allows the detection of impact flashes on the dark side of the Moon. The digital processing unit (DPU) uses powerful event-detection software, and in impact flash search operations the DPU will reduce the data stream dramatically by transmitting only those portions of images that contain events.

Table 5
SELMA orbiter and SIP-MA in situ particle instrument performances.

Instrument	LIS-SW	LIS-MS	LSHE	LES	LEMS	LDD	IPEI
Target	Positive ions	Positive ions (M ≥ 2)	H^+, H^-	Electrons	Neutral	Dust	H^+, e^-
Energy/speed range	1 eV–10 keV	1 eV–1 keV	25 eV–40 keV	<15 keV	0–10 eV	> 1 km/s	< 15 keV
Energy resolution	15%	25%	7%	10%	N/A		10%
FOV	360°×90° (2π)	360°×90° (2π)	360°×90° (2π)	4π	360°×10°		4π for each
Angular resolution	22.5 × 11.25°	22.5 × 11.25°	22.5 × 5°	22.5 × 5°	N/A		22.5 × 5°
Sensitivity, G-factor	10^{-3} cm^2 sr eV/eV	Flux of 10^4/cm^2 s	10^{-2} cm^2 sr		1/cm^3 s		
Time resolution	2s	3s		0.5s	1–100s	0.1s	0.5s
Mass range		2–150 amu			1–1000 amu		N/A
Mass resolution		>80			1100		N/A
Impact charge range						3×10^3–10^7 e–	
Impact charge uncertainty						10%	
Cumulative charge deposition rate						5×10^4 e^-/s	

Table 6
SELMA orbiter and SIP-MA field sensor performance.

Instrument	MMAG	Orchestra	IPMAG	Mini-EF
Platform	Orbiter	Orbiter	SIP-MA	SIP-MA
Target	Magnetic field	Electric field	Magnetic field	Electric field
Range	±64000 nT	DC–1.4 MHz	±10000 nT	DC–1.4 MHz
Resolution	8 pT			
Sensitivity	< 10 pT/√Hz		< 20 pT/√Hz	
Electron density		10-4–105 cm-3		
Electron temperature		0.01–100 eV		

4.3. Moon UV imaging spectrograph (MUVS)

MUVS is a long-slit ultraviolet imaging spectrograph, with a spectral bandpass including far- and mid-ultraviolet wavelengths in the 115–315 nm range, which will be used to: 1) Measure the surface water frost abundance in permanently shadowed regions; 2) Characterize the diurnal transport of water/hydration across the lunar surface; 3) Identify space weathering processes by surveying lunar swirl features; and 4) Investigate the exospheric response to SELMA's impact probes and also natural meteor streams. MUVS builds upon the legacy of LAMP's UV spectral mapping (Gladstone et al., 2010) with the improved sensitivity, spatial resolution, and spectral coverage. By extending the wavelength to 315 nm compared to LRO/UVS), we will search for OH (308 nm) in the exosphere, as well as other components (Mg at 285 nm, Fe at 272 nm, and Si at 252 nm).

The MUVS telescope feeds a 15-cm Rowland circle spectrograph with a spectral bandpass of 115–315 nm. The telescope has an input aperture 4 × 4 cm^2 and uses an off-axis parabolic (OAP) primary mirror. Light from the OAP is focused onto the spectrograph entrance slit, which has field-of-view of 0.3° × 7.5°. Light entering the slit is dispersed by a toroidal diffraction grating that focuses the UV bandpass onto a curved microchannel plate (MCP) cross strip (XS) detector. The MCP uses atomic layer deposition (ALD) coated borosilicate glass plates with a solar blind, UV-sensitive GaN photocathode applied to enable mid-UV sensitivity; a sealed tube vacuum and MgF2 window are used to keep this photocathode pristine, post-assembly.

4.4. ENA telescope (ENAT)

The ENA telescope (ENAT) is based on the CENA (Chandrayaan-1 Energetic Neutrals Analyzer) and ENA (Energetic Neutrals Analyzer) instruments for the Chandrayaan-1 and BepiColombo missions (Barabash et al., 2009; Saito et al., 2010). ENAT has a factor-of-10 better angular resolution and a factor-of-10 larger geometrical factor than them. Signal processing is a heritage from the SWIM (Solar Wind Monitor) sensor on Chandrayaan-1 (Barabash et al. 2009).

ENAT consists of four building blocks, a charged particle deflection and collimator system, a surface ionization section, an energy analyzer and a time-of-flight section. The charged particle deflection and collimator section rejects charged particles up to 10 s keV by electrostatic deflection. As opposed to its predecessors, ENAT features only one single viewing pixel with 5° × 5° angular pixel size, but with a much larger geometric factor. The generated positive ions are extracted from the conversion surface, energy analyzed in a wave shaped energy analyzer and post-accelerated by 2.4 kV. Ions are then guided to the time-of-flight section of the instrument where they hit a highly polished tungsten single crystal surface. The interaction with the surface generates a secondary electron that is measured using a channel electron multiplier (CEM), providing the start signal for the time-of-flight measurement. The ion is most likely neutralized in the process and travels to the stop surface located a short distance away where another secondary electron is generated. This electron is collected by another CEM providing the stop signal of the time-of-flight measurement. The combination of time-of-flight section and the energy of the particle allow us to calculate the mass of the particle.

4.5. Lunar positive ion spectrometer (LIS)

The Lunar positive ion spectrometer (LIS) consists of two sensors: a) the Ion Spectrometer for Solar Wind (LIS-SW) and b) Ion Spectrometer for Mass Spectrometry (LIS-MS). The Cluster/CIS/HIA and CODIF, Cassini/CAPS, BepiColombo/MEA and MSA, Solar Orbiter/SWA/PAS, and JUICE/PEP/JDC sensors provide significant heritage for LIS.

The LIS-SW sensor consists of one compact, low mass, highly capable sensor based on a design carefully and specifically optimized for the ion bulk properties (density, velocity and temperature) of the solar wind. The sensors providing fast 3-D measurements in the energy range 1 eV–10 keV are customized for the energy range as well as the dynamic range encompassing solar wind as well as magnetospheric suprathermal and thermal plasma originating from the Earth when the Moon is embedded within the terrestrial magnetosphere. The LIS-SW sensor consists of five main structural elements: 1) the electrostatic entrance deflector selects incident positively charged particles entering at elevation angle and steers them into the electrostatic analyzer; 2) the electrostatic analyzer selects the energy passband by setting voltages on an inner plate; 3) the detector board includes 16 ceramic CEM along the periphery; 4) the HVPS and FPGA boards situated below the detector plane; 5) an electronic box containing LVPS and DPU boards common to both LIS-SW and LIS-MS contains the rest of the subsystems.

LIS-MS sensor will provide lunar surface and exospheric composition information through secondary ion mass spectrometry. It will measure the secondary ions sputtered from the regolith grains by solar wind ion bombardment. The LIS-MS resolves lunar secondary ion fluxes ranging between ~10 and 10^4 ions cm^{-2} s^{-1} (depending on the species) but excluding high solar wind proton flux and photon background.

The LIS-MS sensor consists of five main structural elements: 1) the electrostatic entrance deflector selects incident positively charged

particles entering at elevation angle and steers them into the filtering chamber; 2) the filtering chamber which should prevent the proton and photon background to enter contaminate the reflectron chamber and let the minor and trace species access the reflectron chamber; 3) the reflection time-of-flight chamber where the selection of ions with m/q is achieved; 4) the HVPS and FPGA boards attached to the sensor head; 5) the electronic box containing LVPS and DPU boards is common to both LIS-SW and LIS-MS.

4.6. Lunar scattered proton and negative ions experiment (LSHE)

LSHE observes and measure the distributions of scattered negative hydrogen, protons and alpha particles in the energy range from 25 eV to 40 keV. The LSHE instrument is based on the design of IMA/MEX, IMA/VEX and ICA on Rosetta. It comprises a top-hat design (16 sectors over 360° entrance) and uses a magnetic mass separation system. Ions entering LSHE first pass through a semi-spherical electrostatic energy analyzer, then a two-slit electrostatic lens, and finally the mass analyzer where a cylindrical magnetic field created by permanent magnets separates the trajectories of different ion species, according to their mass per charge. The particles are detected by an MCP which comprises an anode system with 32 rings representing ion mass.

4.7. Lunar electron spectrometer (LES)

The LES instrument will determine the electron density, temperature and the velocity distribution functions of the local plasma environment of the spacecraft. The baseline design will address this with two top-hat type electrostatic analysers, each with a FoV deflector system to allow electrostatic deflection of incoming electrons by up to ±45° out of the plane of the undeflected FoV. The two sensors will be accommodated on the nadir and zenith faces, close to the edges or corners of the spacecraft.

Incoming charged particles enter the sensor through the exterior electrically grounded aperture grid. The particles are steered from the arrival direction into the hemispheric energy analysis (EA) section using voltages applied to either the upper or lower deflector electrodes providing a field-of-view deflection system. The EA section permits only electrons of the selected energy and type to reach the detector subsystem consisting of a micro-channel plate (MCP) detector.

4.8. Moon magnetometer (MMAG)

The MMAG instrument measures the magnetic field in the vicinity of the spacecraft. This is crucial for characterizing lunar magnetic anomalies and revealing how they interact with the ambient collisionless plasma environment (solar wind as well as the Earth's magnetosheath and magnetotail). Previous implementations of the fluxgate sensors and associated electronics have flown on missions such as Cassini and Double Star, and are included in the planned Solar Orbiter and JUICE magnetic field investigations, providing highly relevant, direct heritage (Dougherty et al., 2004; Carr et al., 2005; O'Brien et al., 2007). Two separate digital fluxgate sensors will perform magnetic field measurements. Fluxgate sensors are electrically passive and comprised of magnetically susceptible cores, each core wrapped by two coils of wire. An alternating current is passed through one coil (the drive coil), cyclically driving the core to positive and negative magnetic saturation. A current proportional to the magnetic field along the coil axis is induced in the other coil (the sense coil). In addition, a current is applied through the sense coil to directly null the detected field along the coil axis through the magnetic core. The combination of current through the three sense coils orthogonal to each other thus allows the full, local magnetic field vector at each fluxgate sensor to be determined.

4.9. Lunar exospheric mass spectrometer (LEMS)

The SELMA neutral gas mass spectrometer (LEMS) is a ToF mass spectrometer using an ion mirror (reflectron) for performance optimization (Wurz et al., 2012). The LEMS mass range is 1–1000 with the resolution of $M/\Delta M = 1100$. The dynamic range is at least 6 decades for a 5 s integration period, allowing for the identification of species down to a partial density of about 1 cm^{-3} in such a measurement.

Ions are either generated in a storage ion source (neutral mode) or collected from the ambient plasma (ion mode). With the pulsed ion optics of the ion source, ion packets are produced, accelerated, shaped and sent into the ToF structure. After passing the first leg of a field-free drift path, ions are reflected by an ion mirror, which allows energy and spatial focusing, and are then directed onto a fast micro-channel plate detector. The charge signal versus time is recorded on the detector, registered by a fast analogue-to-digital converter (ADC) system, and converted into a mass spectrum. A ToF mass spectrometer has inherent advantages with respect to other mass spectrometer concepts since it allows recording of a complete mass spectrum at once without the necessity of scanning over the mass range of interest (Wiley and McLaren, 1955). This results in superior efficiency over scanning instruments (i.e., magnetic sector instruments and quadrupole mass analyzers) and is particularly useful during transient lunar phenomena, where only a short time span is available to perform the mass spectrometric measurements. The LEMS design benefits from heritage from the RTOF sensor of the ROSINA instrument on the Rosetta mission as well as a stratospheric balloon in summer 2008 (Abplanalp et al., 2009; Wieser et al., 2009b).

4.10. Plasma wave instrument (Orchestra)

The instrument Orchestra will monitor the full electric field vector in the frequency range DC up to 1.4 MHz, which will facilitate measurements of a wide range of plasma and electromagnetic waves, including static electric structures, as well as monitoring signals for sampling micrometeoroid impacts, and the spacecraft potential. In addition, Orchestra can also be run in so-called Langmuir mode, and in so doing sample the cold plasma density and integrated EUV flux. These parameters will provide the basis to a) characterize the electric field strength and structure including related acceleration and energization processes within mini-magnetospheres near surface of the Moon (e.g. acceleration structures, Alfvén or whistler wave processes, ion and electron cyclotron waves, boundary processes, reconnection); b) characterize the ambient size/mass distribution of μm-sized dust around the Moon; c) characterize the cold plasma environment; and d) monitor the spacecraft potential for use by the particle instruments.

Two Langmuir probe sensors sample electric voltages or currents, which are the basis of the inferred physical parameters. The probes can therefore be operated in two different modes: current sampling mode (used as Langmuir probes) for plasma diagnostics (e.g., electron and ion densities, electron temperature, and the drift speed) or voltage sampling mode (used as electric field probes) for measurement of the electric field. The spacecraft potential is always measured independent of operation mode. It is important to have both probes extended as far as possible from each other and from spacecraft structures. The 3 m long booms, properly accommodated, facilitate this.

4.11. Lunar dust detector (LDD)

LDD is an in situ dust detector to map the variability of the spatial and size distribution of dust near the Moon. It is a 'built-to-print' version of the Lunar Dust Experiment (LDEX) that flew onboard NASA's LADEE mission from September 2013 to April 2014 (Horányi et al., 2015). LDD will provide complementary observations by a) verifying LDEX results; b) extending the timeline of observations of the dust ejecta production during different meteoroid streams; c) extending the spatial coverage using SELMA's polar orbit; and d) enabling correlation studies between dust influx/production, with the variability of the neutral and plasma environment to be measured by the rest of the SELMA payload.

The detection of a dust particle is based on measuring the charge

generated by its hypervelocity (v > 1 km s^{-1}) impact on a target. The impact charge Q (the total number of ions or electrons) is a function of both the speed v, and the mass m, of the impacting dust particle

$$Q = \alpha m v^{\beta}$$

where the charge is measured in C, the mass in kg, and the speed in km s^{-1}. The speed exponent is in the range $3.5 \leq \beta \leq 5.6$. For a characteristic value of $\beta = 3.5$, $\alpha \sim 0.5$. The values for both α and β are determined by calibrating individual instruments as they depend on the composition of both the impactor and the target, and the geometry of the setup (Horányi et al., 2014).

4.12. Waves and electric field (MiniEF on SIP-MA)

Mini-EF on board the SIP-MA makes use of similar electronics as the Orchestra instrument, but different type of 4 booms and associated 4 Langmuir probe sensors. The MiniEF will use shorter sticks (75 cm), smaller spheres and the pre-amplifiers are within the electric box but the operation principle is similar to Orchestra instrument. MiniEF will not operate in Langmuir mode.

4.13. Impact probe ions and electrons spectrometer (IPEI on SIP-MA)

IPEI is going to measure the properties of the ions and electrons in the magnetic anomalies. The design and the detection principle is the same as the LES instrument which is described above (inverse polarities for the ion detector).

4.14. Impact probe magnetometer (IPMAG on SIP-MA)

The SELMA Impact Probe Magnetometer IPMAG is based on the digital fluxgate magnetometer SMILE (e.g. Forslund et al., 2008, Belyayev and Ivchenko, 2015). It is a miniature flux-gate system with volume compensation sensor, providing magnetic field measurements at a rate of up to 250 Hz, with 16-bit resolution. IPMAG is built around a digital implementation of the correlation loop, implemented in Field Programmable Field Array (FPGA), where the digital samples from the sense coils are processed in a matched filter to produce the digital value of the compensation current. The SMILE magnetometer has been flown on a number of sub-orbital flights (e.g. NASA's Cascades-2 sounding rocket, SNSB's SPIDER sounding rocket) and is qualified to fly on the SEAM nanosatellite in 2017 (realized as EU FP7 project under grant agreement 607197).

The IPMAG instrument will consist of two three-axis fluxgate sensors mounted at different distances from the spacecraft on a 2 m long boom, and electronics inside the impactor. Using one boom for both sensors decreases the influence of spacecraft magnetic interference on the accuracy of the measurements. The 2 m long deployable boom for the two magnetometers is a modification of the dual-tip deployable boom for the SEAM satellite (Mao et al., 2017). Counter-rotating tape spring spools are deployed along with the boom tip. The IPMAG boom design uses the same type of tape springs and spools as the SEAM boom.

4.15. Context cameras (IPCAM on SIP-MA, IECAM on RCS)

IPCAM and IECAM are ordinary RGB cameras that will be mounted on SIP-MA and RCS for video streaming. The main objectives are the context imaging, helping to define the attitude determination, and PR purposes.

4.16. Impactor

The impactor for the impact experiment in the Shackleton crater is a copper sphere of 10 kg (13 cm in diameter). The impactor is passive and does not carry any systems. The spherical shape ensures the independence of the impact on the impactor attitude. The copper is selected to identify the impactor's elements in the volatile plume.

5. Discussion and summary

The SELMA mission investigating the interactions between the surface, exosphere, plasma and dust aims at a launch in 2029–2030 under the ESA's medium-size mission (M5) of the Cosmic Vision programme. SELMA addresses two Cosmic Vision themes; "1. What are the conditions for planet formation and the emergence of life?" and "2. How does the Solar System work?" (Cosmic Vision, 2005). In particular, SELMA focuses the Cosmic Vision topics "1.3 Life and habitability in the Solar System" and "2.3 Asteroids and other small bodies".

SELMA is a unique mission to investigate the complex local space environment–surface interactions. No missions with similar objectives and payload were, are, or will be conducted or planned in the near future. The NASA LADEE mission (Lunar Atmosphere, Dust Environment Explorer, 2013–2014) did not carry the full set of remote sensing instruments and plasma, field, and wave investigations. NASA ARTEMIS (two spacecraft for plasma and field measurements), which is currently in-orbit around the Moon, is not equipped with the instrumentation to characterize the surface properties, exosphere, and dust. Currently, the NASA LRO (Lunar Reconnaissance Orbiter) focuses on remote sensing but lack instrumentation for in situ and remote measurements of the local space environment. The Indian Chandrayaan-1 mission (October 2008–August 2010) with ESA funded science payloads served as a pathfinder for the SELMA mission and demonstrated that the SELMA mission concept is feasible. SELMA will not only perform similar measurements using superior instruments, but it will also characterize the dynamic exosphere and dust environment.

In term of the surface properties and the interaction with the environment, the Moon and Mercury are similar. Although the Mercury has global magnetic field, it has similar physical processes in terms of the interactions between exosphere, plasma and surface because of the lack of the atmosphere (e.g. Milillo et al., 2005; Lue et al., 2017). The influence of the plasma to the surface, which could vary, sputter and weather the surface does happen both at Moon and Mercury. Due to the different interplanetary dust particle speeds (Christou et al., 2015), the parameter range of the observations can be extended, and we can better know the effects of dust impacts on environment. From these comparative aspects into account, the Moon serves as a test-bed in the Earth's backyard to study these processes and better explore and understand the BepiColombo data. ESA BepiColombo will reach Mercury in 2024 and is planned to be operation until 2027. The active data analysis will continue for at least 5 years. The SELMA results, available in 2030, will come very timely to provide the key knowledge for BepiColombo data interpretation to understand the Mercury's exosphere and its variability, the role of the surface in refilling the magnetosphere via ion backscattering and sputtering, and the influence of the environment on the IR and UV surface characteristics. SELMA is a mission of comparative planetology.

The impact experiments SELMA will perform are completely unique. Unprecedented fly-through of a mini-magnetosphere and high time resolution measurements down to the surface have never been even attempted before. The impact experiment in the permanently shadowed Shackleton crater is the first of its kind. The NASA LCROSS mission (Lunar Crater Observation and Sensing Satellite) in 2009 only used remote sensing to investigate the debris plume. SELMA will use in-situ instruments, in particular its powerful mass spectrometer, to directly sample volatiles released during the impact. Due to its position almost at the South Pole and sufficiently high rims, the Shackleton crater to be investigated by the SELMA impact experiment is one of the most interesting locations for future lunar exploration missions.

Research on the SELMA scientific theme is of importance for both fundamental planetary sciences, for our general understanding of how the Solar System works, and for future lunar explorations, through qualitative characterization of the lunar environment and, in particular, investigation of the presence of water in the lunar soil, as a valuable

resource to harvest from the lunar regolith. Determining the water content in the crater's soil is critical for decisions on South Pole exploration.

Acknowledgement

The SELMA proposal team acknowledges the financial support from the Swedish National Space Board (SNSB) for the mission analysis conducted by OHB, Sweden.

Appendix A. SELMA proposal team members

The SELMA mission was proposed to ESA in response to the call for the medium-size mission opportunity (M5). The proposal team members are listed below.

Lead proposer: Stas Barabash (Swedish Institute of Space Physics, Kiruna, Sweden)
Science lead: Yoshifumi Futaana (Swedish Institute of Space Physics, Kiruna, Sweden)

Principal Investigators:

Peter Wurz (University of Bern, Bern, Switzerland)
Mihaly Horanyi (Laboratory for Atmospheric and Space Physics, University of Colorado, USA)
Urs Mall (Max Planck Institute for Solar System Research, Göttingen, Germany)
Martin Wieser (Swedish Institute of Space Physics, Kiruna, Sweden)
Nicolas Andre (IRAP- Université de Toulouse, CNRS, France)
Nickolay Ivchenko (KTH Royal Institute of Technology, Stockholm, Sweden)
Jürgen Oberst (German Aerospace Center, Berlin, Germany)
Kurt Retherford (Southwest Research Institute, San Antonio, USA)
Andrew Coates (Mullard Space Science Laboratory, University College London, London, UK)
Adam Masters (Imperial College London, London, UK)
Jan-Erik Wahlund (Swedish Institute of Space Physics, Uppsala, Sweden)
Esa Kallio (Aalto University, Helsinki, Finland)

Co-Investigators:

M. Holmström, X.-D. Wang, G. Nicolaou, G. S. Wieser, H. Nilsson, S. Fatemi (Swedish Institute of Space Physics, Kiruna, Sweden); A. Vorburger (University of Bern, Bern, Switzerland); A. Fedorov (IRAP, Toulouse, France); A. Margonis, S. Elgner (DLR, Berlin, Germany); J. Bergman, D. Andrews, M. André, S. Buchert, M. Morooka, N. Edberg, A. Eriksson (Swedish Institute of Space Physics, Uppsala, Sweden); Z. Sternovsky, J. Deca (Laboratory for Atmospheric and Space Physics, University of Colorado, USA), J. Szalay (Southwest Research Institute, San Antonio, USA); W. Schmidt (Finnish Meteorological Institute, Helsinki, Finland); Charles Lue (Department of Physics and Astronomy, University of Iowa, USA); O. Korablev, A. Ivanov, A. Fedorova, R. Kuzmin; V. Izmodenov (Space Research Institute, Moscow, Russia); C. M. Pieters (Brown University, Providence, Rhode Island, USA); K. Szego, S. Sandor, Z. Nemeth (Wigner Research Center for Physics, Institute for Particle and Nuclear Physics, Budapest, Hungary); R. Green (Jet Propulsion Laboratory, Pasadena, California, USA); R. C. Clark (US Geological Survey, Denver, Colorado, USA); M. Banaszkiewicz M. Bzowski (Space Research Ceneter, Warsaw, Poland); L. Roth (Royal Institute of Technology, Stockholm, Sweden); I. Mann (EISCAT scientific association, Kiruna, Sweden); K. Dhiren (Mullard Space Science Laboratory, University College London, London, UK); M. Grande (Aberystwyth University, UK); D. Hurley (The Johns Hopkins University Applied Physics Laboratory, Laurel, USA).

References

Abplanalp, D., Wurz, P., Huber, L., Leya, I., Kopp, E., Rohner, U., Wieser, M., Kalla, L., Barabash, S., 2009. A neutral gas mass spectrometer to measure the chemical composition of the stratosphere. Adv. Space Res. 44 (7), 870–878. https://doi.org/10.1016/j.asr.2009.06.016.

Anderson, B.J., Johnson, C.L., Korth, H., Purucker, M.E., Winslow, R.M., Slavin, J.A., Solomon, S.C., McNutt, R.L., Raines, J.M., Zurbuchen, T.H., 2011. The global magnetic field of Mercury from Messenger orbital observations. Science 333 (6051), 1859–1862. https://doi.org/10.1126/science.1211001.

Arnold, J.R., 1979. Ice in the lunar polar regions. J. Geophys. Res. 84 (B10), 5659–5668. https://doi.org/10.1029/JB084iB10p05659.

Barabash, S., Bhardwaj, A., Wieser, M., Sridharan, R., Kurian, T., Varier, S., Vijaykumar, E., Abhirami, V., Raghavendra, K.V., Mohankumar, S.V., Dhanya, D.B., Thampi, S., Asamura, K., Andersson, H., Futaana, Y., Holmström, M., Lundin, R., Svensson, J., Karlsson, S., Piazza, R.D., Wurz, P., 2009. Investigation of the solar wind-Moon interaction on board Chandrayaan-1 mission with the SARA experiment. Curr. Sci. 96 (4), 526–532.

Bellot Rubio, L. R., J. L. Ortiz, and P. V. Sada, Observation and interpretation of meteoroid impact flashes on the moon, in Leonid Storm Research, edited by P. Jenniskens, F. Rietmeijer, N. Brosch, and M. Fonda, pp. 575–598, Springer Netherlands, Dordrecht, doi: 10.1007/978-94-017-2071-7_42, 2000.

Belyayev, S., Ivchenko, N., 2015. Digital fluxgate magnetometer: design notes. Meas. Sci. Technol. 26 (12) https://doi.org/10.1088/0957-0233/26/12/125901, 125,901.

Benna, M., Mahaffy, P.R., Halekas, J.S., Elphic, R.C., Delory, G.T., 2015. Variability of helium, neon, and argon in the lunar exosphere as observed by the LADEE NMS instrument. Geophys. Res. Lett. 42 (10), 3723–3729. https://doi.org/10.1002/2015GL064120.

Berg, O., Wolf, H., Rhee, J., 1976. Lunar soil movement registerd by the Apollo 17 cosmic dust experiment. In: Elsässer, H., Fechting, H. (Eds.), Interplanetary Dust and Zodiacal Light, Lecture Notes in Physics, vol. 48. Springer Berlin/Heidelberg, pp. 233–237. https://doi.org/10.1007/3-540-07615-8_486.

Bruck Syal, M., Schultz, P.H., 2015. Cometary impact effects at the moon: implications for lunar swirl formation. Icarus 257, 194–206. https://doi.org/10.1016/j.icarus.2015.05.005.

Carr, C., Brown, P., Zhang, T.L., Gloag, J., Horbury, T., Lucek, E., Magnes, W., O'Brien, H., Oddy, T., Auster, U., Austin, P., Aydogar, O., Balogh, A., Baumjohann, W., Beek, T., Eichelberger, H., Fornacon, K.-H., Georgescu, E., Glassmeier, K.-H., Ludlam, M., Nakamura, R., Richter, I., 2005. The Double Star magnetic field investigation: instrument design, performance and highlights of the first year's observations. Ann. Geophys. 23 (8), 2713–2732. https://doi.org/10.5194/angeo-23-2713-2005.

Christou, A.A., Killen, R.M., Burger, M.H., 2015. The meteoroid stream of comet encke at Mercury: implications for MErcury surface, space ENvironment, GEochemistry, and ranging observations of exosphere. Geophys. Res. Lett. 42, 7311–7318. https://doi.org/10.1002/2015GL065361.

Clark, R.N., 2009. Detection of adsorbed water and hydroxyl on the Moon. Science 326 (5952), 562–564. https://doi.org/10.1126/science.1178105.

Cocks, F.H., Klenk, P.A., Watkins, S.A., Simmons, W.N., Cocks, J.C., Cocks, E.E., Sussingham, J.C., 2002. Lunar ice: adsorbed water on subsurface polar dust. Icarus 160 (2), 386–397. https://doi.org/10.1006/icar.2002.6972.

Colaprete, A., Schultz, P., Heldmann, J., Wooden, D., Shirley, M., Ennico, K., Hermalyn, B., Marshall, W., Ricco, A., Elphic, R.C., Goldstein, D., Summy, D.,

Bart, G.D., Asphaug, E., Korycansky, D., Landis, D., Sollitt, L., 2010. Detection of water in the LCROSS ejecta plume. Science 330 (6003), 463–468. https://doi.org/10.1126/science.1186986.
Coleman Jr., P.J., Russel, C.T., Sharp, L.R., Schubert, G., 1972. Preliminary mapping of the lunar magnetic field. Phys. Earth Planet. Inter. 6, 167–174. https://doi.org/10.1016/0031-9201(72)90050-7.
Cook, J.C., Alan Stern, S., 2014. Sporadic increases in lunar atmospheric helium detected by lamp. Icarus 236, 48–55. https://doi.org/10.1016/j.icarus.2014.02.001.
Cook, J.C., Stern, S.A., Feldman, P.D., Gladstone, G.R., Retherford, K.D., Tsang, C.C.C., 2013. New upper limits on numerous atmospheric species in the native lunar atmosphere. Icarus 225 (1), 681–687. https://doi.org/10.1016/j.icarus.2013.04.010.
Crider, D.H., Vondrak, R.R., 2000. The solar wind as a possible source of lunar polar hydrogen deposits. J. Geophys. Res. 105 (E11), 26,773–26,782. https://doi.org/10.1029/2000JE001277.
Crider, D.H., Vondrak, R.R., 2002. Hydrogen migration to the lunar poles by solar wind bombardment of the Moon. Adv. Space Res. 30 (8), 1869–1874. https://doi.org/10.1016/S0273-1177(02)00493-3.
Crider, D.H., Vondrak, R.R., 2003. Space weathering effects on lunar cold trap deposits. J. Geophys. Res. 108 (E7), 5079,. https://doi.org/10.1029/2002JE002030.
Criswell, D.R., 1973. Horizon-glow and the motion of lunar dust. In: Grard, R.J.L. (Ed.), Photon and Particle Interactions with Surfaces in Space. Springer. https://doi.org/10.1007/978-94-010-2647-5\s\do5(3)6.
Deca, J., Divin, A., Lembège, B., Horányi, M., Markidis, S., Lapenta, G., 2015. General mechanism and dynamics of the solar wind interaction with lunar magnetic anomalies from 3-d particle-in-cell simulations. J. Geophys. Res. 120 (8), 6443–6463. https://doi.org/10.1002/2015JA021070.
Dougherty, M.K., Kellock, S., Southwood, D.J., Balogh, a., Smith, E.J., Tsurutani, B.T., Gerlach, B., Glassmeier, K.-H., Gleim, F., Russell, C.T., Erdos, G., Neubauer, F.M., Cowley, S.W.H., 2004. The cassini magnetic field investigation. Space Sci. Rev. vol. 114 (1–4), 331–383. https://doi.org/10.1007/s11214-004-1432-2.
Dyadechkin, S., Kallio, E., Wurz, P., 2015. New fully kinetic model for the study of electric potential, plasma, and dust above lunar landscapes. J. Geophys. Res. 120 (3), 1589–1606. https://doi.org/10.1002/2014JA020511.
Dyal, P., Parkin, C.W., Sonett, C.P., 1970. Apollo 12 magnetometer: measurement of a steady magnetic field on the surface of the moon. Science 169 (3947), 762–764. https://doi.org/10.1126/science.169.3947.762.
Elphic, R.C., Hine, B., Delory, G.T., Salute, J.S., Noble, S., Colaprete, A., Horanyi, M., Mahaffy, P., 2014. And the LADEE Science Team, the lunar atmosphere and dust environment explorer (LADEE): initial science results. In: 45th Lunar and Planetary Science Conference, p. 2677.
Fatemi, S., Holmström, M., Futaana, Y., Lue, C., Collier, M.R., Barabash, S., Stenberg, G., 2014. Effects of protons reflected by lunar crustal magnetic fields on the global lunar plasma environment. J. Geophys. Res. https://doi.org/10.1002/2014JA019900.
Fatemi, S., Lue, C., Holmström, M., Poppe, A.R., Wieser, M., Barabash, S., Delory, G.T., 2015. Solar wind plasma interaction with Gerasimovich lunar magnetic anomaly. J. Geophys. Res. 120 (6), 4719–4735. https://doi.org/10.1002/2015JA021027.
Feldman, P.D., Hurley, D.M., Retherford, K.D., Gladstone, G.R., Stern, S.A., Pryor, W., Parker, J.W., Kaufmann, D.E., Davis, M.W., Versteeg, M.H., 2012. Temporal variability of lunar exospheric helium during January 2012 from LRO/LAMP. Icarus 221 (2), 854–858. https://doi.org/10.1016/j.icarus.2012.09.015.
Feldman, P.D., Glenar, D.A., Stubbs, T.J., Retherford, K.D., Randall Gladstone, G., Miles, P.F., Greathouse, T.K., Kaufmann, D.E., Parker, J.W., Alan Stern, S., 2014. Upper limits for a lunar dust exosphere from far-ultraviolet spectroscopy by LRO/LAMP. Icarus 233, 106–113. https://doi.org/10.1016/j.icarus.2014.01.039.
Feldman, W.C., Maurice, S., Binder, A.B., Barraclough, B.L., Elphic, R.C., Lawrence, D.J., 1998. Fluxes of fast and epithermal neutrons from Lunar Prospector: evidence for water ice at the lunar poles. Science 281 (5382), 1496–1500. https://doi.org/10.1126/science.281.5382.1496.
Flynn, B., Mendillo, M., 1993. A picture of the Moon's atmosphere. Science 261 (5118), 184–186. https://doi.org/10.1126/science.261.5118.184.
Forslund, Å., Belyayev, S., Ivchenko, N., Olsson, G., Edberg, T., Marusenkov, A., 2008. Miniaturized digital fluxgate magnetometer for small spacecraft applications. Meas. Sci. Technol. 19 (1) https://doi.org/10.1088/0957-0233/19/1/015202, 015,202.
Fraeman, A.A., Murchie, S.L., Arvidson, R.E., Clark, R.N., Morris, R.V., Rivkin, A.S., Vilas, F., 2014. Spectral absorptions on phobos and deimos in the visible/near infrared wavelengths and their compositional constraints. Icarus 229 (0), 196–205. https://doi.org/10.1016/j.icarus.2013.11.021.
Futaana, Y., Barabash, S., Wieser, M., Holmström, M., Lue, C., Wurz, P., Schaufelberger, A., Bhardwaj, A., Dhanya, M.B., Asamura, K., 2012. Empirical energy spectra of neutralized solar wind protons from the lunar regolith. J. Geophys. Res. 117 (E5) https://doi.org/10.1029/2011JE004019. E05005.
Futaana, Y., Barabash, S., Wieser, M., Lue, C., Wurz, P., Vorburger, A., Bhardwaj, A., Asamura, K., 2013. Remote energetic neutral atom imaging of electric potential over a lunar magnetic anomaly. Geophys. Res. Lett. 40, 262–266. https://doi.org/10.1002/grl.50135.
Garrick-Bethell, I., Head III, J.W., Pieters, C.M., 2011. Spectral properties, magnetic fields, and dust transport at lunar swirls. Icarus 212 (2), 480–492. https://doi.org/10.1016/j.icarus.2010.11.036.
Gladstone, G.R., Stern, S.A., Retherford, K.D., Black, R.K., Slater, D.C., Davis, M.W., Versteeg, M.H., Persson, K.B., Parker, J.W., Kaufmann, D.E., Egan, A.F., Greathouse, T.K., Feldman, P.D., Hurley, D., Pryor, W.R., Hendrix, A.R., 2010. LAMP: the Lyman alpha mapping project on NASA's Lunar Reconnaissance Orbiter mission. Space Sci. Rev. 150 (1), 161–181. https://doi.org/10.1007/s11214-009-9578-6.
Gladstone, G.R., Retherford, K.D., Egan, A.F., Kaufmann, D.E., Miles, P.F., Parker, J.W., Horvath, D., Rojas, P.M., Versteeg, M.H., Davis, M.W., Greathouse, T.K., Slater, D.C., Mukherjee, J., Steffl, A.J., Feldman, P.D., Hurley, D.M., Pryor, W.R., Hendrix, A.R., Mazarico, E., Stern, S.A., 2012. Far-ultraviolet reflectance properties of the Moon's permanently shadowed regions. J. Geophys. Res. 117 https://doi.org/10.1029/2011JE003913.
Glenar, D.A., Stubbs, T.J., Hahn, J.M., Wang, Y., 2014. Search for a high-altitude lunar dust exosphere using clementine navigational star tracker measurements. J. Geophys. Res. 119 (12), 2548–2567. https://doi.org/10.1002/2014JE004702.
Grava, C., Retherford, K.D., Hurley, D.M., Feldman, P.D., Gladstone, G.R., Greathouse, T.K., Cook, J.C., Stern, S.A., Pryor, W.R., Halekas, J.S., Kaufmann, D.E., 2016. Lunar exospheric helium observations of LRO/LAMP coordinated with ARTEMIS. Icarus 273, 36–44. https://doi.org/10.1016/j.icarus.2015.10.033.
Grün, E., Zook, H.A., Fechtig, H., Giese, R.H., 1985. Collisional balance of the meteoritic complex. Icarus 62 (2), 244–272. https://doi.org/10.1016/0019-1035(85)90121-6.
Grün, E., Horanyi, M., Sternovsky, Z., 2011. The lunar dust environment. Planet. Space Sci. 59 (14), 1672–1680. https://doi.org/10.1016/j.pss.2011.04.005.
Halekas, J., Delory, G., Brain, D., Lin, R., Mitchell, D., 2008. Density cavity observed over a strong lunar crustal magnetic anomaly in the solar wind: a mini-magnetosphere? Planet. Space Sci. 56 (7), 941–946. https://doi.org/10.1016/j.pss.2008.01.008.
Halekas, J.S., Poppe, A.R., Delory, G.T., Sarantos, M., McFadden, J.P., 2013. Using ARTEMIS pickup ion observations to place constraints on the lunar atmosphere. J. Geophys. Res. 118 (1), 81–88. https://doi.org/10.1029/2012JE004292.
Halekas, J.S., Benna, M., Mahaffy, P.R., Elphic, R.C., Poppe, A.R., Delory, G.T., 2015. Detections of lunar exospheric ions by the LADEE neutral mass spectrometer. Geophys. Res. Lett. 42 (13), 5162–5169. https://doi.org/10.1002/2015GL064746.
Hartle, R.E., Killen, R., 2006. Measuring pickup ions to characterize the surfaces and exospheres of planetary bodies: applications to the Moon. Geophys. Res. Lett. 33 (5) https://doi.org/10.1029/2005GL024520 n/a–n/a.
Heiken, G.H., Vaniman, D.T., French, B.M. (Eds.), 1991. Lunar Sourcebook: a User's Guide to the Moon. Cambridge University Press.
Hendrix, A.R., Retherford, K.D., Randall Gladstone, G., Hurley, D.M., Feldman, P.D., Egan, A.F., Kaufmann, D.E., Miles, P.F., Parker, J.W., Horvath, D., Rojas, P.M., Versteeg, M.H., Davis, M.W., Greathouse, T.K., Mukherjee, J., Steffl, A.J., Pryor, W.R., Stern, S.A., 2012. The lunar far-UV albedo: indicator of hydration and weathering. J. Geophys. Res. 117 (E12) https://doi.org/10.1029/2012JE004252 n/a–n/a.
Hinton, F., Taeusch, D., 1964. Variation of the lunar atmosphere with the strength of the solar wind. J. Geophys. Res. 69 (7), 1341–1347. https://doi.org/10.1029/JZ069i007p01341.
Hodges, J., Richard, R., 2002. Ice in the lunar polar regions revisited. J. Geophys. Res. 107 (E2) https://doi.org/10.1029/2000JE001491.
Hodges, R.R., 1991. Exospheric transport restrictions on water ice in lunar polar traps. Geophys. Res. Lett. 18 (11), 2113–2116. https://doi.org/10.1029/91GL02533.
Hodges, R.R., 2011. Resolution of the lunar hydrogen enigma. Geophys. Res. Lett. 38 https://doi.org/10.1029/2011GL046688. L06201.
Hodges, R.R., 2016. Methane in the lunar exosphere: implications for solar wind carbon escape. Geophys. Res. Lett. 43 (13), 6742–6748. https://doi.org/10.1002/2016GL068994.
Hodges, R.R., Johnson, F.S., 1968. Lateral transport in planetary exospheres. J. Geophys. Res. 73 (23), 7307–7317. https://doi.org/10.1029/JA073i023p07307.
Hodges Jr., R.R., Hoffman, J.H., 1975. Implications of atmospheric Ar-40 escape on the interior structure of the moon. Lunar Planet. Sci. Conf. Proc. Lunar Planet. Sci. Conf. Proc. 6, 3039–3047.
Hodges, R.R.J., Hoffman, J.H., Johnson, F.S., Evans, D.E., 1973. Composition and dynamics of lunar atmosphere. Lunar Planet. Sci. Conf. Proc. 1142, 374–375.
Hood, L.L., Huang, Z., 1991. Formation of magnetic anomalies antipodal to lunar impact basins: two-dimensional model calculations. J. Geophys. Res. 96 (B6), 9837–9846. https://doi.org/10.1029/91JB00308.
Hood, L.L., Coleman Jr., P.J., Wilhelms, D.E., 1979. Lunar nearside magnetic anomalies. In: Hinners, N.W. (Ed.), Lunar and Planetary Science Conference Proceedings, Lunar and Planetary Science Conference Proceedings, vol. 10, pp. 2235–2257.
Hood, L.L., Zakharian, A., Halekas, J., Mitchell, D.L., Lin, R.P., Acuña, M.H., Binder, A.B., 2001. Initial mapping and interpretation of lunar crustal magnetic anomalies using Lunar Prospector magnetometer data. J. Geophys. Res. 106 (E11), 27,825–27,839. https://doi.org/10.1029/2000JE001366.
Horányi, M., Sternovsky, Z., Lankton, M., Dumont, C., Gagnard, S., Gathright, D., Grün, E., Hansen, D., James, D., Kempf, S., Lamprecht, B., Srama, R., Szalay, J.R., Wright, G., 2014. The lunar dust experiment (LDEX) onboard the lunar atmosphere and dust environment explorer (LADEE) mission. Space Sci. Rev. 185 (1), 93–113. https://doi.org/10.1007/s11214-014-0118-7.
Horányi, M., Szalay, J.R., Kempf, S., Schmidt, J., Grun, E., Srama, R., Sternovsky, Z., 2015. A permanent, asymmetric dust cloud around the Moon. Nature 522 (7556), 324–326. https://doi.org/10.1038/nature14479.
Housen, K.R., Holsapple, K.A., 2011. Ejecta from impact craters. Icarus 211 (1), 856–875. https://doi.org/10.1016/j.icarus.2010.09.017.
Hunten, D.M., Cremonese, G., Sprague, A.L., Hill, R.E., Verani, S., Kozlowski, R.W.H., 1998. The Leonid meteor shower and the lunar sodium atmosphere. Icarus 136 (2), 298–303. https://doi.org/10.1006/icar.1998.6023.
Hurley, D.M., Cook, J.C., Benna, M., Halekas, J.S., Feldman, P.D., Retherford, K.D., Hodges, R.R., Grava, C., Mahaffy, P., Gladstone, G.R., Greathouse, T., Kaufmann, D.E., Elphic, R.C., Stern, S.A., 2016. Understanding temporal and spatial variability of the lunar helium atmosphere using simultaneous observations from LRO, LADEE, and ARTEMIS. Icarus 273, 45–52. https://doi.org/10.1016/j.icarus.2015.09.011.
Hurley, D.M., Cook, J.C., Retherford, K.D., Greathouse, T., Gladstone, G.R., Mandt, K., Grava, C., Kaufmann, D., Hendrix, A., Feldman, P.D., Pryor, W., Stickle, A., Killen, R.M., Stern, S.A., 2017. Contributions of solar wind and micrometeoroids to molecular hydrogen in the lunar exosphere. Icarus 31–37. https://doi.org/10.1016/j.icarus.2016.04.019.

Iglseder, H., Uesugi, K., Svedhem, H., 1996. Cosmic dust measurements in lunar orbit. Adv. Space Res. 17 (12), 177–182. https://doi.org/10.1016/0273-1177(95)00777-C.
Imamura, T., Iwata, T., ichi Yamamoto, Z., Mochizuki, N., Kono, Y., Matsumoto, K., Liu, Q., Noda, H., Harada, H., Ichiro Oyama, K., Nabatov, A., Futaana, Y., Saito, A., Ando, H., 2010. Studying the lunar ionosphere with SELENE Radio Science experiment. Space Sci. Rev. https://doi.org/10.1007/s11214-010-9660-0.
Jarvinen, R., Alho, M., Kallio, E., Wurz, P., Barabash, S., Futaana, Y., 2014. On vertical electric fields at lunar magnetic anomalies. Geophys. Res. Lett. 41 (7), 2243–2249. https://doi.org/10.1002/2014GL059788.
Johnson, F.S., 1971. Lunar atmosphere. Rev. Geophys. 9 (3), 813–823. https://doi.org/10.1029/RG009i003p00813.
Kallio, E., Jarvinen, R., Dyadechkin, S., Wurz, P., Barabash, S., Alvarez, F., Fernandes, V.A., Futaana, Y., Harri, A.-M., Heilimo, J., Lue, C., Mäkelä, J., Porjo, N., Schmidt, W., Siili, T., 2012. Kinetic simulations of finite gyroradius effects in the lunar plasma environment on global, meso, and microscales. Planet. Space Sci. 74 (1), 146–155. https://doi.org/10.1016/j.pss.2012.09.012.
Kallio, E., Dyadechkin, S., Fatemi, S., Holmström, M., Futaana, Y., Wurz, P., Fernandes, V.A., Álvarez, F., Heilimo, J., Jarvinen, R., Schmidt, W., Harri, A.M., Barabash, S., Mäkelä, J., Porjo, N., Alho, M., 2016. Dust environment of an airless object: a phase space study with kinetic models. Planet. Space Sci. 120, 56–69. https://doi.org/10.1016/j.pss.2015.11.006.
Killen, R.M., Burger, M.H., Farrell, W.M., 2017. Exospheric escape: a parametrical study. Adv. Space Res. https://doi.org/10.1016/j.asr.2017.06.015 in Press.
Kirsch, E., Wilken, B., Gloeckler, G., Galvin, A., Geiss, J., Hovestadt, D., 1998. Search for lunar pickup ions. In: COSPAR Colloquia Series, vol. 9. Elsevier, pp. 65–69. https://doi.org/10.1016/S0964-2749(98)80011-5.
Krüger, H., Krivov, A., Grün, E., 2000. A dust cloud of Ganymede maintained by hypervelocity impacts of interplanetary micrometeoroids. Planet. Space Sci. 48 (15), 1457–1471. https://doi.org/10.1016/S0032-0633(00)00092-1.
Lanzerotti, L.J., Brown, W.L., Johnson, R.E., 1981. Ice in the polar regions of the moon. J. Geophys. Res. 86 (B5), 3949–3950. https://doi.org/10.1029/JB086iB05p03949.
Li, S., Milliken, R.E., 2017. Water on the surface of the moon as seen by the moon mineralogy mapper: distribution, abundance, and origins. Sci. Adv. 3 https://doi.org/10.1126/sciadv.1701471 e1701471.
Lin, R.P., Mitchell, D.L., Curtis, D.W., Anderson, K.A., Carlson, C.W., McFadden, J., Acuña, M.H., Hood, L.L., Binder, A., 1998. Lunar surface magnetic fields and their interaction with the solar wind: results from Lunar Prospector. Science 281 (5382), 1480–1484. https://doi.org/10.1126/science.281.5382.1480.
Lord, H.C., 1968. Hydrogen and helium ion implantation into olivine and enstatite: retention coefficients, saturation concentrations, and temperature-release profiles. J. Geophys. Res. 73 (16), 5271–5280.
Lue, C., Futaana, Y., Barabash, S., Wieser, M., Holmström, M., Bhardwaj, A., Dhanya, M., Wurz, P., 2011. Strong influence of lunar crustal fields on the solar wind flow. Geophys. Res. Lett. 38 (3) https://doi.org/10.1029/2010GL046215. L03202.
Lue, C., Futaana, Y., Barabash, S., Wieser, M., Bhardwaj, A., Wurz, P., 2014. Chandrayaan-1 observations of backscattered solar wind protons from the lunar regolith: dependence on the solar wind speed. J. Geophys. Res. 119, 968–975. https://doi.org/10.1002/2013JE004582.
Lue, C., Futaana, Y., Barabash, S., Wieser, M., Bhardwaj, A., Wurz, P., Asamura, K., 2017. Solar wind scattering from the surface of Mercury: lessons from the moon. Icarus 296, 39–48. https://doi.org/10.1016/j.icarus.2017.05.019.
Mall, U., Kirsch, E., Cierpka, K., Wilken, B., Söding, A., Neubauer, F., Gloeckler, G., Galvin, A., 1998. Direct observation of lunar pick-up ions near the Moon. Geophys. Res. Lett. 25 (20), 3799–3802. https://doi.org/10.1029/1998GL900003.
Mall, U., Banaszkiewicz, M., Brønstad, K., McKenna-Lawlor, S., Nathues, A., Søraas, F., Vilenius, E., Ullaland, K., 2009. Near infrared spectrometer SIR-2 on Chandrayaan-1. Curr. Sci. 96 (4), 506–511.
Mangano, V., Milillo, A., Mura, A., Orsini, S., De Angelis, E., Di Lellis, A.M., Wurz, P., 2007. The contribution of impulsive meteoritic impact vapourization to the Hermean exosphere. Planet. Space Sci. 55 (11), 1541–1556. https://doi.org/10.1016/j.pss.2006.10.008.
Mao, H., Ganga, P.L., Ghiozzi, M., Ivchenko, N., Tibert, G., 2017. Deployment of bistable self-deployable tape spring booms using a gravity offloading system. J. Aerosp. Eng. 30 (4) https://doi.org/10.1061/(ASCE)AS.1943-5525.0000709, 04017,007.
McCord, T.B., Taylor, L.A., Combe, J.P., Kramer, G., Pieters, C.M., Sunshine, J.M., Clark, R.N., 2011. Sources and physical processes responsible for OH/H2O in the lunar soil as revealed by the Moon Mineralogy Mapper (M3). J. Geophys. Res. 116 https://doi.org/10.1029/2010JE003711. E00G05.
McCoy, J.E., 1976. Photometric studies of light scattering above the lunar terminator from Apollo solar corona photography. In: Proc. Lunar Sci. Conf. 7th, pp. 1087–1112.
McCoy, J.E., Criswell, D.R., 1974. Evidence for a high altitude distribution of lunar dust. In: Proceedings of the Fifth Lunar Conference, Supplement 5, Ceochimica et Cosmochimica Acta, vol. 3, pp. 2991–3005.
Mendillo, M., Baumgardner, J., 1995. Constraints on the origin of the Moon's atmosphere from observations during a lunar eclipse. Nature 377 (6548), 404–406. https://doi.org/10.1038/377404a0.
Milillo, A., Wurz, P., Orsini, S., Delcourt, D., Kallio, E., Killen, R.M., Lammer, H., Massetti, S., Mura, A., Barabash, S., Cremonese, G., Daglis, I.A., Angelis, E., Lellis, A.M., Livi, S., Mangano, V., Torkar, K., 2005. Surface-exosphere-magnetosphere system of Mercury. Space Sci. Rev. 117 (3), 397–443. https://doi.org/10.1007/s11214-005-3593-z.
Mitrofanov, I.G., Sanin, A.B., Boynton, W.V., Chin, G., Garvin, J.B., Golovin, D., Evans, L.G., Harshman, K., Kozyrev, A.S., Litvak, M.L., Malakhov, A., Mazarico, E., McClanahan, T., Milikh, G., Mokrousov, M., Nandikotkur, G., Neumann, G.A., Nuzhdin, I., Sagdeev, R., Shevchenko, V., Shvetsov, V., Smith, D.E., Starr, R., Tretyakov, V.I., Trombka, J., Usikov, D., Varenikov, A., Vostrukhin, A., Zuber, M.T., 2010. Hydrogen mapping of the lunar south pole using the LRO neutron detector experiment LEND. Science 330 (6003), 483–486. https://doi.org/10.1126/science.1185696.
Murphy, D., Vondrak, R., 1993. Effects of levitated dust on astronomical observations from the lunar surface, American Astronomical Society, 182nd AAS Meeting, id.51.21. Bull. Am. Astronomical Soc. 25, 1033.
Ness, N.F., Behannon, K.W., Lepping, R.P., Whang, Y.C., Schatten, K.H., 1974. Magnetic field observations near Mercury: preliminary results from Mariner 10. Science 185 (4146), 151–160. https://doi.org/10.1126/science.185.4146.151.
Oberst, J., Flohrer, J., Elgner, S., Maue, T., Margonis, A., Schrödter, R., Tost, W., Buhl, M., Ehrich, J., Christou, A., Koschny, D., 2011. The smart panoramic optical sensor head (SPOSH)—a camera for observations of transient luminous events on planetary night sides. Planet. Space Sci. 59 (1), 1–9. https://doi.org/10.1016/j.pss.2010.09.016.
O'Brien, H., Brown, P., Beek, T., Carr, C., Cupido, E., Oddy, T., 2007. A radiation tolerant digital fluxgate magnetometer. Meas. Sci. Technol. 18 (11), 3645,. https://doi.org/10.1088/0957-0233/18/11/050.
Ong, L., Asphaug, E.I., Korycansky, D., Coker, R.F., 2010. Volatile retention from cometary impacts on the Moon. Icarus 207 (2), 578–589. https://doi.org/10.1016/j.icarus.2009.12.012.
Pieters, C.M., Goswami, J.N., Clark, R.N., Annadurai, M., Boardman, J., Buratti, B., Combe, J.P., Dyar, M.D., Green, R., Head, J.W., Hibbitts, C., Hicks, M., Isaacson, P., Klima, R., Kramer, G., Kumar, S., Livo, E., Lundeen, S., Malaret, E., McCord, T., Mustard, J., Nettles, J., Petro, N., Runyon, C., Staid, M., Sunshine, J., Taylor, L.A., Tompkins, S., Varanasi, P., 2009. Character and spatial distribution of OH/H2O on the surface of the Moon seen by M3 on Chandrayaan-1. Science 326 (5952), 568–572. https://doi.org/10.1126/science.1178658.
Poppe, A.R., Fatemi, S., Garrick-Bethell, I., Hemingway, D., Holmström, M., 2016. Solar wind interaction with the reiner gamma crustal magnetic anomaly: connecting source magnetization to surface weathering. Icarus 266, 261–266. https://doi.org/10.1016/j.icarus.2015.11.005.
Potter, A., Morgan, T., 1988. Discovery of sodium and potassium vapor in the atmosphere of the Moon. Science 241 (4866), 675–680. https://doi.org/10.1126/science.241.4866.675.
Potter, A., Morgan, T., 1998. Coronagraphic observations of the lunar sodium exosphere near the lunar surface. J. Geophys. Res. 103 (E4), 8581–8586. https://doi.org/10.1029/98JE00059.
Purucker, M.E., Head, J.W., Wilson, L., 2012. Magnetic signature of the lunar south pole-aitken basin: character, origin, and age. J. Geophys. Res. 117 (E5) https://doi.org/10.1029/2011JE003922.
Rennilson, J., Criswell, D.R., 1974. Surveyor observations of lunar horizon-glow. Earth, Moon, Planets 10, 121–142. https://doi.org/10.1007/BF00655715.
Richmond, N.C., Hood, L.L., 2008. A preliminary global map of the vector lunar crustal magnetic field based on Lunar Prospector magnetometer data. J. Geophys. Res. 113 (E2) https://doi.org/10.1029/2007JE002933.
Russell, C.T., Lichtenstein, B.R., 1975. On the source of lunar limb compressions. J. Geophys. Res. 80 (34), 4700–4711. https://doi.org/10.1029/JA080i034p04700.
Saito, Y., Sauvaud, J.A., Hirahara, M., Barabash, S., Delcourt, D., Takashima, T., Asamura, K., 2010. Scientific objectives and instrumentation of Mercury plasma particle experiment (MPPE) onboard mmo. Planet. Space Sci. 58 (1–2), 182–200. https://doi.org/10.1016/j.pss.2008.06.003.
Saito, Y., Nishino, M.N., Fujimoto, M., Yamamoto, T., Yokota, S., Tsunakawa, H., Shibuya, H., Matsushima, M., Shimizu, H., Takahashi, F., 2012. Simultaneous observation of the electron acceleration and ion deceleration over lunar magnetic anomalies. Earth Planets Space 64, 83–92. https://doi.org/10.5047/eps.2011.07.011.
Sprague, A.L., Kozlowski, R.W.H., Hunten, D.M., Wells, W.K., Grosse, F.A., 1992. The sodium and potassium atmosphere of the Moon and its interaction with the surface,. Icarus 96 (1), 27–42. https://doi.org/10.1016/0019-1035(92)90004-Q.
Stern, S.A., 1999. The lunar atmosphere: history, status, current problems, and context. Rev. Geophys. 37 (4), 453–491. https://doi.org/10.1029/1999RG900005.
Stern, S.A., Cook, J.C., Chaufray, J.Y., Feldman, P.D., Gladstone, G.R., Retherford, K.D., 2013. Lunar atmospheric H2 detections by the LAMP UV spectrograph on the lunar reconnaissance orbiter. Icarus 226 (2), 1210–1213. https://doi.org/10.1016/j.icarus.2013.07.011.
Sternovsky, Z., Chamberlin, P., Horanyi, M., Robertson, S., Wang, X., 2008. Variability of the lunar photoelectron sheath and dust mobility due to solar activity. J. Geophys. Res. 113 (A10) https://doi.org/10.1029/2008JA013487.
Stubbs, T.J., Vondrak, R.R., Farrell, W.M., 2006. A dynamic fountain model for lunar dust. Adv. Space Res. 37 (1), 59–66. https://doi.org/10.1016/j.asr.2005.04.048.
Stubbs, T.J., Glenar, D.A., Farrell, W.M., Vondrak, R.R., Collier, M.R., Halekas, J.S., Delory, G.T., 2011. On the role of dust in the lunar ionosphere. Planet. Space Sci. 59 (13), 1659–1664. https://doi.org/10.1016/j.pss.2011.05.011.
Sunshine, J.M., Farnham, T.L., Feaga, L.M., Groussin, O., Merlin, F., Milliken, R.E., A'Hearn, M.F., 2009. Temporal and spatial variability of lunar hydration as observed by the Deep Impact spacecraft. Science 326 (5952), 565–568. https://doi.org/10.1126/science.1179788.
Szalay, J.R., Horányi, M., 2015. The search for electrostatically lofted grains above the Moon with the Lunar Dust Experiment. Geophys. Res. Lett. 42 (13), 5141–5146. https://doi.org/10.1002/2015GL064324.
Taylor, A.D., 1996. Earth encounter velocities for interplanetary meteoroids. Adv. Space Res. 17 (12), 205–209. https://doi.org/10.1016/0273-1177(95)00782-A.
Thompson II, M., 1968. The energy spectrum of ejected atoms during the high energy sputtering of gold. Philos. Mag. 18, 377–414. https://doi.org/10.1080/14786436808227358.
Tsunakawa, H., Takahashi, F., Shimizu, H., Shibuya, H., Matsushima, M., 2015. Surface vector mapping of magnetic anomalies over the Moon using Kaguya and Lunar

Prospector observations. J. Geophys. Res. 120 (6), 1160–1185. https://doi.org/10.1002/2014JE004785.
Vondrak, R.R., 1983. Lunar Base Activities and the Lunar Environment, vol. 1. NASA, Johnson Space Center, pp. 337–345.
Vorburger, A., Wurz, P., Barabash, S., Wieser, M., Futaana, Y., Holmström, M., Bhardwaj, A., Asamura, K., 2012. Energetic neutral atom observations of magnetic anomalies on the lunar surface. J. Geophys. Res. 117 (A7) https://doi.org/10.1029/2012JA017553. A07,208.
Vorburger, A., Wurz, P., Barabash, S., Wieser, M., Futaana, Y., Lue, C., Holmström, M., Bhardwaj, A., Dhanya, M.B., Asamura, K., 2013. Energetic neutral atom imaging of the lunar surface. J. Geophs. Res. 118 (7), 3937–3945. https://doi.org/10.1002/jgra.50337.
Vorburger, A., Wurz, P., Barabash, S., Wieser, M., Futaana, Y., Holmström, M., Bhardwaj, A., Asamura, K., 2014. First direct observation of sputtered lunar oxygen. J. Geophys. Res. 119 (2), 709–722. https://doi.org/10.1002/2013JA019207.
Wang, X., Howes, C.T., Horányi, M., Robertson, S., 2013. Electric potentials in magnetic dipole fields normal and oblique to a surface in plasma: understanding the solar wind interaction with lunar magnetic anomalies. Geophys. Res. Lett. 40 (9), 1686–1690. https://doi.org/10.1002/grl.50367.
Watson, K., Murray, B.C., Brown, H., 1961. The behavior of volatiles on the lunar surface,. J. Geophys. Res. 66 (9), 3033–3045. https://doi.org/10.1029/JZ066i009p03033.
Wieczorek, M.A., Weiss, B.P., Stewart, S.T., 2012. An impactor origin for lunar magnetic anomalies. Science 335 (6073), 1212–1215. https://doi.org/10.1126/science.1214773.
Wieler, R., Kehm, K., Meshik, A.P., Hohenberg, C.M., 1996. Secular changes in the xenon and krypton abundances in the solar wind recorded in single lunar grains. Nature 384 (6604), 46–49. https://doi.org/10.1038/384046a0.
Wieser, M., Barabash, S., Futaana, Y., Holmström, M., Bhardwaj, A., Sridharan, R., Dhanya, M.B., Wurz, P., Schaufelberger, A., Asamura, K., 2009a. Extremely high reflection of solar wind protons as neutral hydrogen atoms from regolith in space. Planet. Space Sci. 57, 2132–2134. https://doi.org/10.1016/j.pss.2009.09.012.
Wieser, M., Kalla, L., Barabash, S., Hedqvist, T., Kemi, S., Widell, O., Abplanalp, D., Wurz, P., 2009b. The Mars Environment Analogue Platform long duration balloon flight. Adv. Space Res. 44 (3), 308–312. https://doi.org/10.1016/j.asr.2009.03.014.
Wieser, M., Barabash, S., Futaana, Y., Holmström, M., Bhardwaj, A., Sridharan, R., Dhanya, M.B., Schaufelberger, A., Wurz, P., Asamura, K., 2010. First observation of a mini-magnetosphere above a lunar magnetic anomaly using energetic neutral atoms. Geophys. Res. Lett. 37 (5) https://doi.org/10.1029/2009GL041721.
Wiley, W.C., McLaren, I.H., 1955. Time-of-flight mass spectrometer with improved resolution. Rev. Sci. Instrum. 26 (12), 1150–1157. https://doi.org/10.1063/1.1715212.
Wilson, J., Mendillo, M., Spence, H., 2006. Magnetospheric influence on the Moon's exosphere. J. Geophys. Res. 111 (A7) https://doi.org/10.1029/2005JA011364. A07,207.
Wurz, P., Rohner, U., Whitby, J.A., Kolb, C., Lammer, H., Dobnikar, P., Martín-Fernández, J.A., 2007. The lunar exosphere: the sputtering contribution. Icarus 191 (2), 486–496. https://doi.org/10.1016/j.icarus.2007.04.034.
Wurz, P., Abplanalp, D., Tulej, M., Lammer, H., 2012. A neutral gas mass spectrometer for the investigation of lunar volatiles. Planet. Space Sci. 74 (1), 264–269. https://doi.org/10.1016/j.pss.2012.05.016.
Yokota, S., Saito, Y., 2005. Estimation of picked-up lunar ions for future compositional remote SIMS analyses of the lunar surface. Earth Planets Space 57, 281–289. https://doi.org/10.1186/BF03352564.
Yurimoto, H., Kuramoto, K., Krot, A.N., Scott, E.R.D., Cuzzi, J.N., Thiemens, M.H., Lyons, J.R., 2007. Origin and evolution of oxygen-isotropic compositions of the solar system. In: Reipurth, B., Jewitt, D., Keil, K. (Eds.), Protostars and Planets V. University of Arizona Press, Tucson, pp. 849–862.
Zimmerman, M.I., Farrell, W.M., Poppe, A.R., 2015. Kinetic simulations of kilometer-scale mini-magnetosphere formation on the Moon. J. Geophys. Res. 120 (11), 1893–1903. https://doi.org/10.1002/2015JE004865.
Zook, H.A., McCoy, J.E., 1991. Large scale lunar horizon glow and a high altitude lunar dust exosphere. Geophys. Res. Lett. 18 (11), 2117. https://doi.org/10.1029/91GL02235.